

Review

Advances of gold nanoclusters for bioimaging

Cheng Zhang,^{1,4} Xiaobing Gao,^{3,4} Wenrui Chen,^{1,4} Meng He,² Yao Yu,² Guanbin Gao,^{1,*} and Taolei Sun^{1,2,*}

SUMMARY

Gold nanoclusters (AuNCs) have become a promising material for bioimaging detection because of their tunable photoluminescence, large Stokes shift, low photobleaching, and good biocompatibility. Last decade, great efforts have been made to develop AuNCs for enhanced imaging contrast and multimodal imaging. Herein, an updated overview of recent advances in AuNCs was present for visible fluorescence (FL) imaging, near-infrared fluorescence (NIR-FL) imaging, two-photon near-infrared fluorescence (TP-NIR-FL) imaging, computed tomography (CT) imaging, positron emission tomography (PET) imaging, magnetic resonance imaging (MRI), and photoacoustic (PA) imaging. The justification of AuNCs applied in bioimaging mentioned above applications was discussed, the performance location of different AuNCs were summarized and highlighted in an unified parameter coordinate system of corresponding bioimaging, and the current challenges, research frontiers, and prospects of AuNCs in bioimaging were discussed. This review will bring new insights into the future development of AuNCs in bio-diagnostic imaging.

INTRODUCTION

Bioimaging, including visible light fluorescence (FL) imaging, near-infrared fluorescence (NIR-FL) imaging, two-photon near-infrared fluorescence (TP-NIR-FL) imaging, computed tomography (CT) imaging, positron emission tomography (PET) imaging, magnetic resonance imaging (MRI), and photoacoustic (PA) imaging, is an indispensable method in biological research and medical diagnosis. They can play important roles in understanding the structure of biological tissues and elucidating the various physiological functions of life. Advances in optical technology, especially the introduction of digital imaging and computer vision techniques, the development of contrast agents with multiple imaging modalities, and the combination of different imaging modalities have improved the efficiency and accuracy of medical diagnosis.

In 1969, the photoluminescence of gold caused by the electronic interband transition was first discovered (Mooradian, 1969). Subsequently, the investigation of FL within the other Au-based materials has been studied. However, the weak FL of Au-based materials was almost undetectable to the naked eye, and their low quantum yields limited further applications in biomedical fields. It was not until 1994 that Brust et al. (1994) proposed a chemical reduction method using alkanethiols as surface ligands and successfully synthesized gold nanoclusters (AuNCs). With the continuous improvement and innovation of the synthesis methods and ligand modifiers of AuNCs, the quantum yield of AuNCs is constantly improving, and some even reach 70% (Wang et al., 2005; Lee et al., 2004). Inspired by these findings, a series of AuNCs protected by various ligands were prepared, and the investigations on the structures, properties and related applications of AuNCs have increased rapidly. As a bridge between Au atoms and gold nanoparticles (AuNPs), AuNCs are ultra-small nanoparticles (NPs) (typically less than 3 nm in diameter) consisting of Au(I)-organic ligand shells with different numbers of Au atoms (Goswami et al. (2016a)). Because of their size comparable to the Fermi wavelength of electrons, AuNCs exhibit molecular-like properties, including intense photoluminescence (PL), molecular chirality, magnetism, and catalysis (Maity et al., 2019; Xu et al., 2019). AuNCs also possess unique optical and electrical properties, including discrete electronic transitions and highest occupied molecular orbital-lowest unoccupied molecular orbital (HOMO-LUMO) energy level transitions (Chan and Nie, 1998; Guo and Wang, 2011). The FL of AuNCs can be influenced by various factors, including the size of the Au nucleus, the type of surface ligands, and the surrounding environment (Zheng et al., 2004; Zhu et al., 2020a). Because of their excellent photostability and biocompatibility, AuNCs have potential uses in biomedical imaging (Du et al., 2018; Xu et al., 2019). As shown in Figure 1, existing common imaging modalities include FL, magnetic resonance (MR), X-ray computed

¹State Key Laboratory of Advanced Technology for Materials Synthesis and Processing, Wuhan University of Technology, 122 Luoshi Road, Wuhan 430070, China

²School of Chemistry, Chemical Engineering and Life Science, Wuhan University of Technology, 122 Luoshi Road, Wuhan 430070, China

³General Hospital of Central Theater Command, Wuhan 430070, China

⁴These authors contributed equally

*Correspondence: gbgao@whut.edu.cn (G.G.), suntl@whut.edu.cn (T.S.)
<https://doi.org/10.1016/j.isci.2022.105022>



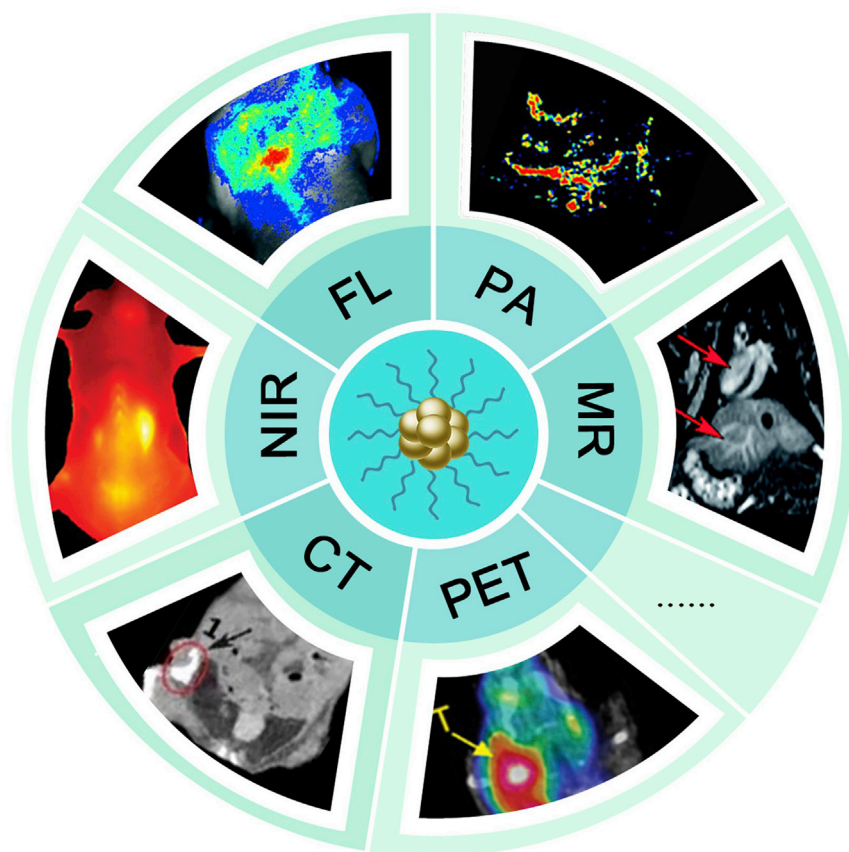


Figure 1. Gold nanoclusters for bioimaging applications

Abbreviations in the figure, FL: Fluorescence; NIR: Near-Infrared; CT: Computed Tomography; PET: Positron Emission Computed Tomography; MR: Magnetic Resonance; PA: Photoacoustic.

tomography (CT), positron emission tomography (PET), and photoacoustic (PA) imaging (Bai et al., 2020; Fu et al., 2019; Werner et al., 2008; Zhang and Wang, 2014).

Although several studies have reviewed the properties and applications of AuNCs, they have primarily focused on the preparation, biosensing, catalysis, and therapeutic applications of AuNCs (Bai et al., 2020; Cui et al., 2014; Porret et al., 2020; Zheng et al., 2021c). As a novel fluorescent material, AuNCs have contributed to many advances in bio-diagnostic imaging. Therefore, in this review, the advantages of AuNCs in imaging applications were first introduced, and the origin of the AuNCs FL mechanism was summarized. Then, a summary of the existing advances in AuNCs was provided for visible FL imaging, near-infrared (NIR) FL imaging, CT imaging, PET imaging, MR imaging (MRI), and PA imaging. In addition, the detailed parameters of AuNCs were summarized for bioimaging applications. Finally, the problems and challenges encountered in using AuNCs for bioimaging were presented, hoping to bring new ideas for future applications of AuNCs in bioimaging.

JUSTIFICATION OF AUNCs FOR BIOIMAGING

AuNCs, whose cores typically consist of unequal numbers of gold atoms, have excellent FL intensity and high X-ray attenuation coefficients, enabling FL and CT imaging. AuNCs can also be loaded with contrast agents for other imaging techniques, such as radionuclides for PET imaging (^{64}Cu , ^{68}Ga , and ^{124}I) or gadolinium chelates for MR contrast. The core is coated with polymers, proteins, or other compounds to enhance its solubility and biocompatibility. The coating can also be loaded with drugs or targeting ligands (antibodies, peptides, nucleic acids, proteins, and aptamers) for integrated diagnosis and therapy. Figure 2A depicts a schematic diagram of AuNCs used as a contrast agent designed for imaging.

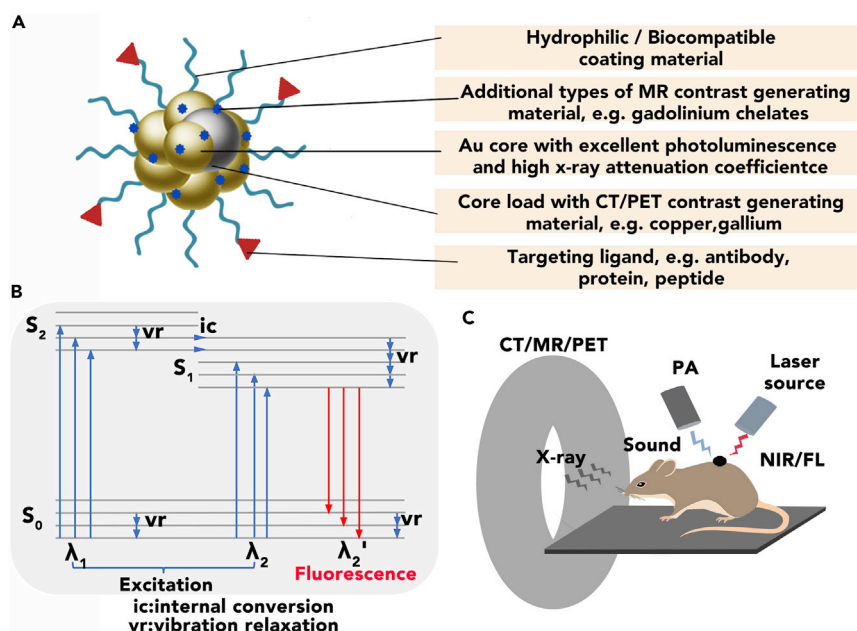


Figure 2. Justification of AuNCs for bioimaging

(A) Generalized schematic depiction of AuNCs used as contrast agent.
 (B) Schematic diagram of AuNCs photoluminescence.
 (C) Schematic illustration of AuNCs enabling *in vivo* multimodal imaging.

Photoluminescence (PL)

PL is one of the most important properties of AuNCs for imaging applications. The large AuNPs have a distinct UV (UV)-visible absorption peak at 520 nm, indicating a surface plasmon resonance absorption. As the size of AuNPs decreases to less than 3 nm, the intensity of the absorption peak of AuNPs near 520 nm gradually decreases or disappears. The absorption peak at a specific wavelength is achieved by leaping electrons between energy levels, showing molecule-like properties, which replace this peak (Chan and Nie, 1998). When light hits AuNCs, electrons are stimulated, resulting in electron leaps between discrete energy levels of radiation churning, resulting in brilliant PL. The basic principle of AuNCs PL is shown in Figure 2B. Li et al. (2019b) proposed a novel explanation for the origin of AuNCs PL by studying a series of AuNCs with a single cuboctahedral core. They claimed that although the surface is necessary for the AuNCs mentioned above to luminesce at room temperature, the internal Au nuclei, rather than the charge transfer at the surface, are the source of the luminescence. The existing studies on the luminescence mechanism of AuNCs do not provide an accurate explanation; therefore, a comprehensive and systematic study of the luminescence mechanism of AuNCs is needed.

Fluorescence

In previous studies, electron leaps between HOMO and LUMO in Au atoms were considered the primary source of FL production in AuNCs (Li et al., 2021; Zhang and Wang, 2014). According to this concept, the FL properties change dramatically when the structure of AuNCs is changed. The FL properties of AuNCs are affected by their sizes and the number of Au atoms. For example, the PL of AuNCs modified by the same molecule changes from the visible region to the near-infrared region, but their Au nuclei consist of a different number of Au atoms (Yu et al., 2013; Zheng et al., 2004). As another example, glutathione (GSH)-modified $Au_{22}(SR)_{18}$ (SR: thiolate) and GSH- $Au_{25}(SR)_{18}$ possess the same type and number of ligands, and their PL properties differ because of the presence of different numbers of Au atoms in these clusters. $Au_{22}(SR)_{18}$ emits an intense red light under UV irradiation, whereas $Au_{25}(SR)_{18}$ shows very weak FL (Yu et al., 2014).

The FL properties of AuNCs also vary with the type and structure of the surface ligands. For example, $Au_{25}(GSH)_{18}$ emits light at 610 nm, whereas $Au_{25}(BSA)_{18}$ (BSA: bovine serum albumin) emits at 640 nm with a 30-nanometer redshift (Kang et al., 2018). Thus, the role of ligands in AuNCs luminescence has received much attention. The factors responsible for the unique FL characteristics of AuNCs are now

characterized as ligand-to-metal charge transfer, ligand-to-metal charge transfer, and electron leap within the Au nuclei (Abbas et al., 2018). All three Au₂₄(SR)₂₀ reported by Gan et al. (2016) exhibited robust red FL, which increased with the intensity of the ligand-electron-donor. The quantum yields of the two Au₂₈(SR)₂₀ modified with different-R groups showed prominent differences, with Au₂₈(CHT)₂₀ (CHT: cyclohexanethiolate) having a more than 15-fold higher PL quantum yield ratio than Au₂₈(TBBT)₂₀ (TBBT: *p*-tert-butylbenzenethiolate). This gap originates from the different structural arrangements of the staple motifs in the shell (Chen et al., 2020).

Phosphorescence

Phosphorescence is a slow luminescence phenomenon originating from radiative transitions between different states. Unlike FL, the luminescence phenomena of phosphorescence remain when the incoming light is turned off. In the aggregated state of [Au₈]⁴⁺, Sugiuchi et al. (2017) discovered the transition of PL emission from FL to phosphorescence. The monomeric cluster emits visible FL at 596 nm, but on aggregation, it emits a second near-infrared peak at 708 nm with a phosphorescent character. Excitation spectroscopy studies revealed that phosphorescent emission originates from exciton-coupled cluster assemblies, which have higher emission activity than monomeric clusters. In addition, significant phosphorescence emission was seen in solid-state clusters, with a quantum efficiency two orders of magnitude higher than that of monomeric clusters in solution. Similarly, the monomeric and solid-state clusters of GSH-AuNCs emitted for 4.3 and 7.9 s, respectively, confirming phosphorescent emission (Pan et al., 2019). Under UV light, the aqueous solution of GSH-AuNCs displayed relatively mild red emission; however, when it was dissolved in an acidic solution or an ethanol solvent, its GSH-AuNCs aggregation was activated, resulting in enhanced red emission.

The self-assembly of AuNCs can be induced and the optical characteristics of AuNCs can be modified by introducing different chemicals. For example, electrostatic and hydrophobic interactions between hyaluronic acid, protamine, and fluorescent AuNCs impair the non-radiative transition of AuNCs, boosting phosphorescence emission (Xia et al., 2019). Shen et al. (2021) prepared L-/D-cysteine modified AuNCs, which self-assemble into highly ordered chiral microflower structures upon Cd²⁺/H⁺ induction, and this compact structure promotes Au(I)-Au(I) interactions and ligand-metal charge transfer (LMCT), resulting in fluorescence-phosphorescence conversion and emission lifetime extension up to 3.34 ms. Furthermore, dual FL and phosphorescence emission was observed in both NCs of Au₁₁Cu₁NCs and Au₁₀Ag₂NCs (Lei et al., 2016; Wu et al., 2021). At present, researchers focus on the study of the phosphorescence properties of AuNCs, and the development of AuNCs phosphorescence imaging probes is still in the development stage.

Two-photon (TP) excitation

Compared to single-photon excitation, nanomaterials with two-photon (TP) excitation can emit high-energy FL by absorbing two relatively low-energy photons, whereas the energy level jump requires only half the energy difference between these two energy levels. Thus, TP excitation is of great benefit in bioimaging. Ramakrishna et al. (2008) produced hexane thiolate-stabilized Au₂₅NCs with good TP absorption (TPA) properties in hexane. According to their results, the TPA cross-section of this cluster was up to 17080 GM, which is close to the theoretical limit. Captopril-or GSH-protected AuNCs also show high TPA absorption (Olesiak-Banska et al., 2016; Polavarapu et al., 2011). Recently, dihydrolipoic acid (DHLA)-coated AuNCs were found to have an even higher TPA cross-section, with a cross-section of 10⁶ GM for the 800 nm emitter (Tian et al., 2021). The extremely high TP cross-section of AuNCs can be used as an excellent bioimaging agent for TP imaging.

Tunable emission

Although the source of AuNCs PL is unknown, various factors affecting the luminescence of AuNCs have been reported. The ability to tune the brightness of AuNCs is an essential feature for their widespread use in bioimaging. Therefore, many strategies for tuning the emission wavelength of AuNCs and increasing their FL intensity have been developed. A list of them is given below.

- (1) Limiting the number of Au atoms in the system. Because AuNCs are the primary source of cluster luminescence, varying the size of AuNCs can control the emission wavelengths. Zheng et al. (2004) synthesized AuNCs with different numbers of Au atoms by varying the concentration of Au³⁺ in the tree-like macromolecule, producing Au₅, Au₈, Au₁₃, Au₂₃ and Au₃₁, resulting in emission spectra from the visible to the NIR region.

- (2) Using different ligands, such as proteins, peptides, deoxyribonucleic acids (DNAs), and polymers (El-Sayed and Schneider, 2020). Studies have suggested that the FL of AuNCs could be enhanced by increasing the ability of the ligand to provide charge and increasing the oxidation state of the metal nuclei (Li et al., 2019b; Wu and Jin, 2010). Groups with electron-rich molecules were also found to promote FL. Kundu et al. (2020) used four different peptide chain lengths of thiol ligands to modify AuNCs, resulting in FL emissions ranging from 510 to 612 nm.
- (3) Rigidifying the nuclear shells of AuNCs. Mixing tetraoctylammonium bromide (TOA) with GSH-AuNCs and pairing the TOA cation with the carboxylic acid heel anion of GSH, the shell layer of AuNCs was rigidified, leading to a 9-fold increase in FL intensity (Pyo et al., 2015, 2016).
- (4) Aggregation-induced emission (AIE). Luo et al. (2012) synthesized Au(I)-SR oligomers with GSH, which did not fluoresce in an aqueous solution. However, after adding enormous amounts of ethanol to the aqueous solution, the Au(I)-SR oligomers fluoresced with different intensities due to aggregation. The link between the length of the Au(I)-SR motifs and the AIE was further investigated, allowing to modify of the emission wavelength of AuNCs by changing the length of the Au(I)-SR motifs (Goswami et al., 2016b; Wu et al., 2020; Yu et al., 2014).
- (5) Doping with other metal ions. For example, using Ag ion doping, Ag/AuNCs with different FL emission and FL intensity can be obtained by controlling the molar ratio of Ag: Au. (Jia et al., 2020; Zhai et al., 2018). Because of the synergistic effect of Ag and AuNCs, doping Ag can improve the FL intensity, and its intensity usually increases first and then decreases with the increase of Ag.

High X-Ray attenuation coefficient

When an X-ray penetrates an item, it interacts with the atoms of the material through absorption and scattering, causing the intensity of the X-ray to be attenuated during transmission. The attenuation coefficient is generally proportional to the atomic number and density of the substance. Compared to the commonly used I, Au has a higher atomic number (Au, 79; I, 53) and X-ray absorption coefficient (at 100 keV: Au, $5.16\text{cm}^2\text{g}^{-1}$; I, $1.94\text{cm}^2\text{g}^{-1}$). The contrast effect of Au is also 2.7-times higher than that of I per unit mass (Hainfeld et al., 2006). Several studies have shown that the K-edge (the minimum energy required to excite the elements in a sample to produce FL X-rays) of Au is 80.7 keV. When Au atoms are irradiated with X-rays of energy 80.7 keV or slightly more significant, their absorption coefficient increases exponentially, resulting in a significant increase in their corresponding attenuation coefficients (Hainfeld et al., 2006). They also pointed out that AuNPs should be prepared at a specific mass concentration when used as a contrast agent. X-ray attenuation increases with the mass concentration of AuNPs. At the same mass concentration, the size of AuNPs significantly affects the X-ray attenuation ability. Smaller AuNCs with larger specific surface areas exhibit more excellent apparent X-ray attenuation, showing their great potential as CT contrast agents (Tsvirkun et al., 2018; Xu et al., 2008).

Magnetism

Au is a diamagnetic element, but it exhibits magnetic characteristics at the nanoscale scale, as revealed by AuNPs (Trudel, 2011). According to research, the magnetism of AuNPs is influenced by their electronic structure, which is connected to their size and surface ligands (Krishna et al., 2014; Trudel, 2011; Ulloa et al., 2021). As a result, researchers are keeping a careful eye on the magnetic characteristics of atomically accurate AuNCs. At ambient temperature, $[\text{Au}_{25}(\text{PPh}_3)_{10}(\text{SC}_{12}\text{H}_{25})_5\text{Cl}_2]^{2+}$ and $\text{Au}_{38}(\text{SC}_{12}\text{H}_{25})_{24}$ are diamagnetic, whereas $\text{Au}_{25}(\text{SC}_2\text{H}_4\text{Ph})_{18}$ is paramagnetic, and $\text{Au}_{55}(\text{PPh}_3)_{12}\text{C}_{16}$ is ferromagnetic (Krishna et al., 2014). And $\text{Au}_{25}(\text{SC}_2\text{H}_4\text{Ph})_{18}$ has varied magnetic characteristics in different solid state. The thin film $\text{Au}_{25}(\text{SC}_2\text{H}_4\text{Ph})_{18}$ exhibits paramagnetic behavior; however, as the temperature decreases, ferromagnetic interaction occurs; the single crystal exhibits ferromagnetism; and when a large number of crystallites exist, it exhibits obvious paramagnetic, superparamagnetic, and ferromagnetic behavior (Agrachev et al., 2017). Li and Jin (2021) recently hypothesized that the magnetic behavior of AuNCs can be predicted using their specific chemical formula (Li and Jin, 2021). They also propose that after adding or withdrawing one electron, AuNCs with an icosahedral core transfer magnetic. Window and Ackerson (2020) discovered charge-dependent paramagnetism in $\text{Au}_{102}(\text{SPh})_{44}$, as well as paramagnetism when two electrons were removed from $\text{Au}_{102}(\text{SPh})_{44}$ (Window and Ackerson, 2020). Zhu et al. (2009) have hypothesized that the magnetism of $\text{Au}_{25}(\text{SR})_{18}$ nanoparticles can be reversed by accurately manipulating their charge state. Although several investigations have been conducted on the formation of magnetism in AuNCs, its origin remains unknown.

Easy surface functionalization

The rational design of AuNCs surface modification ligands can further expand the biological applications of AuNCs. Surface functionalization of AuNCs can be divided into in-synthesis functionalization and post-synthesis functionalization (Song et al., 2016). In-synthesis functionalization, namely, the addition of pre-designed ligands during the synthesis process. Many studies have used different types of molecules with good biocompatibility, such as small organic molecules, amino acids, proteins, peptides, DNAs, and polymers (Zhu et al., 2020b). These ligands not only act as stabilizers but also greatly improve the properties of AuNCs by increasing their PL wavelengths, conferring targeting properties and treating diseases such as cancer (Gao et al., 2019; Li et al., 2019a). In addition, increasing the targeting of AuNCs can greatly improve the contrast and accuracy of the imaging site. Because tumor cells highly express receptors on their surface, modification of AuNCs using targeting molecules such as folic acid (FA) and various antibodies enable tumor cell-specific imaging (Hada et al., 2021; Zhou et al., 2013).

Functionalization after synthesis is usually based on ligand exchange, bioconjugation and non-covalent interactions (Zheng et al., 2017). Ligand exchange is one of the most commonly used strategies for functionalizing AuNCs. Through ligand exchange, the optical and electronic properties of AuNCs can be modified. A typical example is the conversion of non-FL AuNPs (AuNPs@DDAB, DDAB: didodecyl-dimethylammonium bromide) into red-emitting AuNCs (AuNCs@DHLA) through ligand exchange (Lin et al., 2009). Fernando and Aikens (2015) studied the reaction kinetics of ligand exchange of AuNCs (Fernando and Aikens, 2015). They found that ligand exchange occurred between-SH and embedded Au atoms. In addition, the structure of AuNCs may change during ligand exchange. The ligand exchange reaction of $[\text{Au}_{11}(\text{PPh}_3)_8\text{Cl}_2]\text{Cl}$ (PPh: triphenylphosphine) with water-soluble arylphosphines synthesized water-soluble $[\text{Au}_9(\text{PPh}_3)_8]^{3+}$, and the phosphine-stabilized Au_{11} reacted with GSH in water under a nitrogen atmosphere to give $\text{Au}_{25}(\text{SG})_{18}$ (Ndugire and Yan, 2021; Shichibu et al., 2005). A series of thiol ligands of different chain lengths were exchanged with GSH-AuNCs ligands to prepare AuNCs of different sizes, which exhibited a tunable emission (Kundu et al., 2020).

Bioconjugation is usually achieved by further modifying other molecules on AuNCs with the modified ligands, mainly through functional group interactions between the two ligands. The standard coupling method is between amine and carboxylate groups activated by N-(3-dimethyl aminopropyl)-N-ethyl carbodiimide (EDC). In the synthesis of AuNCs, stabilizers with exemplary terminal functional groups, such as alcohols, carboxylic acids, primary amines and thiols, are usually selected to prevent the aggregation of AuNCs. Then superior biomolecules are further selected to couple with them to achieve multi-functionalization of AuNCs (Song et al., 2016; Wang et al., 2017; Zheng et al., 2017). For example, FA is conjugated to GSH capped AuNCs to achieve targeted recognition of cancer cells (Zhang et al., 2013). Anti-human immunoglobulin E (IgE) is coupled to lipoic acid-modified fluorescent AuNCs to measure IgE in human serum (Alonso et al., 2016). Horseradish peroxidase (HRP)-coupled AuNCs are internalized by breast cancer cells, generating free radicals and inducing apoptosis (Vivo-Llorca et al., 2022).

Non-covalent interactions are also an effective strategy for the functionalization of AuNCs. For example, through electrostatic interactions, lysozyme (Lys)-AuNCs-curcumin (Cur) couples can bind to bacteria for real-time imaging of bacteria with excellent antibacterial effects (Zhang et al., 2022). In addition, the quantum yield of AuNCs was significantly improved by hardening the Au(I)-thiol salt shells with TOA cations (Pyo et al., 2015).

Easy to doping

Doping with other metals can significantly improve the physicochemical properties of homogeneous AuNCs. As previously stated, FL emission can be tuned and FL intensity can be increased. Doping other metals in AuNCs is thus a useful method of tailoring the structure and properties of nanoclusters (Kang et al., 2020). The position of the doping of the doped metal is related to its kind by investigating the detailed structure of the doped clusters (Jin et al., 2016). Alkan et al. (2019) investigated the doping theory of clusters such as Au_{24} and Au_{37} and discovered that the X group elements (Ni, Pd, and Pt) prefer the center position, and the radius of the doping metal can greatly impact the geometry of the alloy clusters and relative stability. For the Au_{25}^{-1} cluster, Pd and Pt tend to be in the center position, Ag tends to the Au core surface, and Cd and Hg tend to the core surface and the ligand shell part (Tian et al., 2016; Yao et al., 2015). For some special AuNCs, Ag can be doped inside the Au core ($\text{Ag}_{46}\text{Au}_{24}$, and $\text{Au}_{57}\text{Ag}_{53}$) (Guan et al., 2018;

Wang et al., 2015b). Kang et al. (2020) provide a detailed description of the structure and behavior of atomic-scale alloy nanoclusters.

Doping allows AuNCs to be used for multimodal imaging. The use of radionuclides (e.g., ^{64}Cu , ^{68}Ga , ^{124}I , etc.) to label AuNCs enables PET and PET/CT imaging and improves the sensitivity of detection (Han et al., 2020a; Sultan et al., 2021; Zheng et al., 2021a). Modification of AuNCs using Gd ions or Gd complexes also enables MRI (Liang and Xiao, 2017; Liang et al., 2013; Sun et al., 2013). Therefore, AuNCs are expected to be ideal multimodal imaging probes (Figure 2C).

Good biocompatibility

After injection, safe and valuable imaging probes must be properly eliminated from the body within a certain period. According to previous studies, AuNCs can enter the body either by injection or oral administration. Once in the body, AuNCs enter many organs through the bloodstream, including the heart, liver, spleen, lungs, kidneys, and brain (Hu et al., 2020; Zhang et al., 2012b). AuNCs are usually absorbed by the liver, secreted with bile, and finally excreted in the urine and feces. Previous studies have shown that specific NPs with hydrodynamic diameters less than 5.5 nm can be efficiently and rapidly cleared by the kidneys (Choi et al., 2007; Du et al., 2018). Chen et al. (2016) observed the renal clearance of ^{64}Cu -labeled AuNCs by dynamic PET imaging of these AuNCs. It was shown that the kidney rapidly cleared synthetic AuNCs with an elimination half-life of <6 min, much shorter than previously reported AuNCs. Because the glomerulus more readily captured smaller AuNCs, a reduction in the size of several atoms also decreased renal clearance efficiency, causing an inverse size-dependent renal clearance of AuNCs in the subnanometer region (Du et al., 2017). The 24-h urinary excretion of kidney-clearable AuNCs around 2 nm was typical > 50% ID, comparable to the renal clearance efficiency of clinically used small molecule probes (Alric et al., 2013; Simpson et al., 2013; Yu and Zheng, 2015; Zhang et al., 2015a; Zhou et al., 2011, 2012). In addition, the modification of different ligands also affects the renal clearance of AuNCs, with GSH-modified AuNCs showing much higher renal clearance over 24 h than BSA-modified AuNCs (Zhang et al., 2012b).

AuNPs have an inert gold nucleus, and therefore AuNPs are usually considered to have good biocompatibility. However, it has been shown that the size of AuNPs affects the cytotoxicity of AuNPs (Schrand et al., 2010). Pan et al. (2007) conducted a systematic study on the cytotoxicity of triphenylphosphine derivative-modified AuNPs with sizes ranging from 0.8 to 15 nm. They found that the cytotoxicity depended on the particle size of AuNPs, and the cytotoxicity of AuNCs was more significant than that of the larger 15 nm AuNPs. They suggested that AuNCs when endocytosed by cells, may interact with cell membranes and thus trigger apoptosis or necrosis of cells. As the particle size decreased, its specific surface area increased, and it was more bioactive, putting it at increased risk of toxicity (Schrand et al., 2010; Yang et al., 2022). This size dependence is also observed in silver thiolated nanoparticles (Yang et al., 2016). In another study, AuNPs of 3–100 nm were injected into mice separately, where AuNPs of 3, 5, 50 and 100 nm showed no deleterious effects. However, AuNPs of 8–37 nm caused severe disease and death in mice within 21 days (Chen et al., 2009). They concluded that AuNPs smaller than 5 nm could be associated with enhanced clearance activity of the immune system, thus reducing the biotoxicity of AuNPs. Also, the ligands on the surface of AuNPs also affected cytotoxicity, and the selection of biocompatible ligands could significantly reduce the cytotoxicity of AuNPs (Peng and Liang, 2019). A large number of experiments have confirmed that the ligand-modified AuNCs have the advantage of low toxicity, and injection into mice will not affect their vital organs. Therefore, AuNCs have excellent biomedical prospects.

ADVANCES OF AUNCS APPLIED IN BIOIMAGING

Visible light fluorescence (FL) imaging

FL imaging has been widely used in the biomedical field to diagnose and guide disease treatment. It is known that fluorescent substances release fluorescent signals when activated by an external light source, and their intensity is proportional to the number of fluorophores in a particular range. AuNCs are widely used for FL imaging because of their robust photostability, photobleaching ability, and tunable luminescence.

Using suitable biomolecules and ligands with different activities, the FL emission wavelength of AuNCs can be modified, and the imaging categories of AuNCs in cells or animals can be identified. Cong et al. (2021) created AuNCs-SP@CS (SP: spiropyran, CS: chitosan) by combining the photoisomerization of SP with the spatially protective ability of CS. Förster resonance energy transfer occurred between the AuNCs and spiropyran for reversible FL modulation with dual emission in the UV/visible light. The clusters entered the

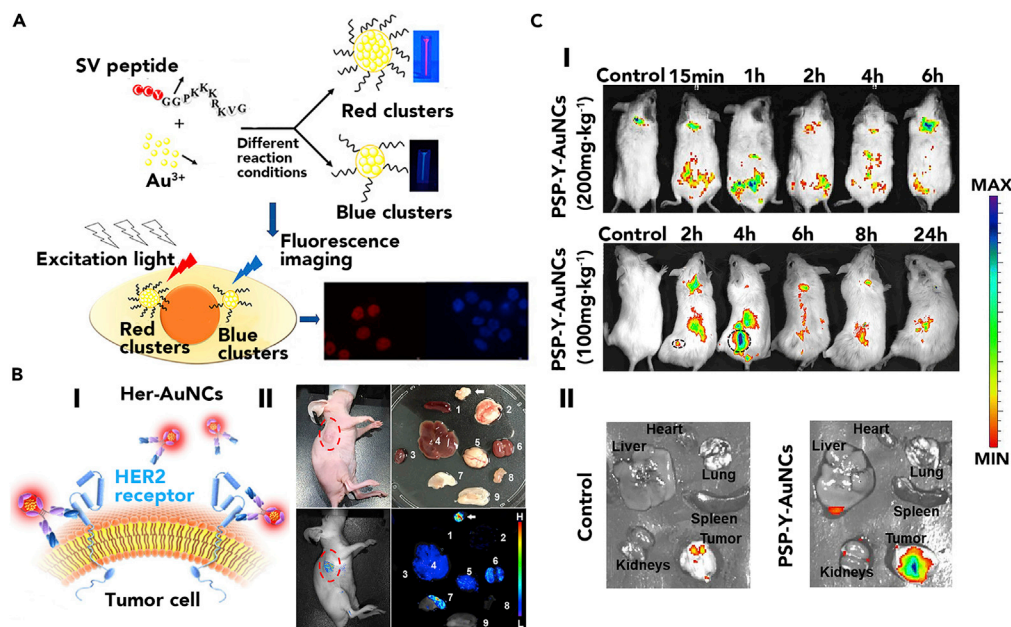


Figure 3. Fluorescence imaging

(A) Schematic diagram of the synthesized peptide template gold nanoclusters with red and blue FL emitted under different synthesis conditions for cell nuclear imaging. Adapted from Ref. (Liu et al., 2020), Copyright (2020), with permission of American Chemical Society.

(B) (I) Schematic representation of Her-AuNCs synthesis and target recognition. (II) Representative images of SKBR3 tumor-bearing nude mice and their tissues under visible light and optical imaging after Her-AuNCs injection. White arrows and red circles indicate tumor locations. Adapted from Ref. (Zhang et al., 2020), Copyright (2020), with permission of American Chemical Society.

(C) Representative images of PSP-Y-AuNCs injected into mice. (I) FL images of PSP-Y-AuNCs (200 and 100 mg kg⁻¹) at different times after injection into HeLa tumor-bearing nude mice. (II) *In vivo* FL images of various organs after 4 h of PSP-Y-AuNCs administration (Ex:430 nm/Em:520 nm). Adapted from Ref. (Raju et al., 2020), Copyright (2020), with permission of Springer-Nature.

nucleus of MCF-7 cells, allowing precise differentiation between the cytoplasm and nucleus within the cell. Liu et al. (2020) prepared red- and blue-light-emitting AuNCs that could target the nucleus for imaging by adjusting the order of modulating pH using the same peptide, as shown in Figure 3A. Yang et al. (2021) prepared GSH-AuNCs, which emitted red FL at a high quantum yield (8.9%) emitting red FL, which was used for brain neuroimaging by current displacement. Endocytosis allows the clusters to enter the cell, where they accumulate in the cytoplasm and undergo some AIE augmentation. They remained stable in mice for up to 21 days and red FL was still visible near the sciatic nerve. AuNCs can monitor the development of amyloid (Kundu et al., 2020; Lai et al., 2016). 16-polymer-nucleoprotein-protected AuNCs (7A-AuNCs) prepared by Lv et al. (2020) were also able to image hazardous substances (methylmercury) in the mouse brain in an acute toxicity model. In addition, persistent FL-specific labeling of tumor cells can be rapidly achieved by *in situ* synthesis of AuNCs in cancer cells (Wang et al., 2013). Zhu et al. (2019) prepared core-shell AuNCs with rigid host-guest components (Prot/MTU-AuNCs) by modifying the antimicrobial agent protamine (Prot) to 6-methyl-2-thiouracil (MTU)-stabilized AuNCs, which greatly enhanced their FL and allowed easy imaging of bacteria.

To enable tumor cell-targeted imaging and recognition of specific receptors on the surface of tumor cells, receptors targeting peptides and antibodies (such as FA) are usually modified on the surface of AuNCs. Feng et al. (2020) used DNA Mucin 1 (MUC1) inducers to target 4T1 cancer cells that recognize mucin over-expression. Zhang et al. (2020) used herceptin, a monoclonal antibody against the human epidermal growth factor 2 (HER2) receptor monoclonal antibody, to stabilize synthetic fluorescent Her-AuNCs. During long-term observations, the synthetic Her-AuNCs showed good specific target recognition imaging of HER2-positive tumors, as shown in Figure 3B. Because cancer cells over-express L-type amino acid transporter proteins, which detect methionine (Met) ligands on the surface of Met-AuNCs, Met-modified AuNCs

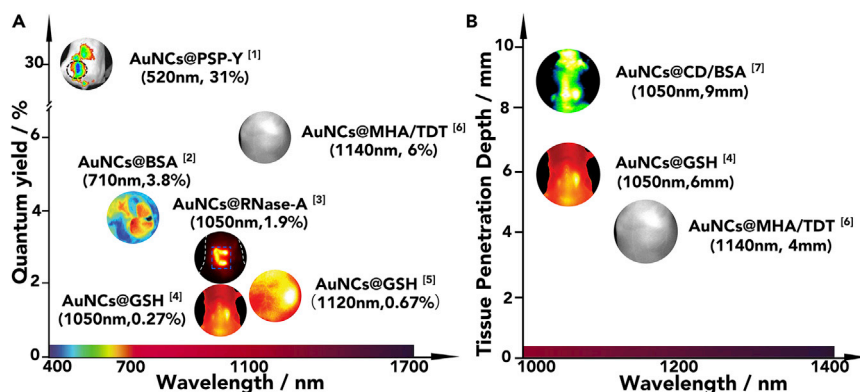


Figure 4. FL imaging of a mouse following intravenous injection of AuNCs

(A) FL quantum yield of different AuNCs. [1] Adapted from Ref. (Raju et al., 2020), Copyright (2020), with permission of Springer-Nature. [2] Adapted from Ref. (Wu et al., 2010), Copyright (2009), with permission of Royal Society of Chemistry. [3] Adapted from Ref. (Wang et al., 2020), Copyright (2020), with permission of John Wiley and Sons. [4] Adapted from Ref. (Li et al., 2020a), Copyright (2020), with permission of John Wiley and Sons. [5] Adapted from Ref. (Liu et al., 2019), Copyright (2019), with permission of John Wiley and Sons. [6] Reprinted with permission from (Yu et al., 2020). Copyright (2020) American Chemical Society.

(B) NIR-II FL images of AuNCs with different tissue depth. [7] Adapted from Ref. (Song et al., 2021), Copyright (2020), with permission of John Wiley and Sons.

are particularly capable of recognizing cancer cells (Pan et al., 2018). Raju et al. (2020) created green-light-emitting AuNCs (PSP-Y-AuNCs) by combining natural polysaccharides (PSP) with L-cysteine (Y), which have a pH-dependent FL emission wavelength value dependence. A blue shift was noted with increasing pH, allowing ratio-metric pH imaging and tumor-targeted imaging (Figure 3C).

BSA is the most commonly used protein in biochemical experiments due to its high stability and biocompatibility. BSA is commonly used as a stabilizer and reducing agent in preparing AuNCs (Hu et al., 2012; Zhang and Han, 2018). *In situ* sequestered BSA-AuNCs synthesized from BSA showed higher FL and quantum yields (about 6%) than NaBH₄ as a reducing agent (Xie et al., 2009). Subsequent studies also confirmed the targeted recognition of tumors by BSA-AuNCs (Zhang et al., 2015b). Compared to BSA-AuNCs, FA-modified BSA-AuNCs showed better-targeted imaging of human ovarian cancer cells and improved cellular uptake due to overexpression of FA receptors in ovarian tumor cells (Hada et al., 2021). Similarly, mannose-modified BSA-AuNCs specifically identified human breast cancer cells (Sha et al., 2020).

In bioimaging, FL in the visible band will be significantly affected because biological tissues have autofluorescence, usually generated by near-UV and blue light excitation (Ballou et al., 2005). Although the FL signal is much more potent than the bioluminescence signal, the signal-to-noise ratio of non-specific FL is significantly lower than that of bioluminescence. Because of this background noise, the sensitivity of FL imaging is limited and challenging to reduce, limiting the application of AuNCs. In addition, visible light is scattered and absorbed when passing through tissues, which limits penetration depth and spatial resolution (Zelmer and Ward, 2013). As a result, FL imaging can only image superficial tissues, resulting in a loss of physiological and pathological information (Leblond et al., 2010).

Near-infrared (NIR) FL imaging

NIR imaging can penetrate deep tissues well, which compensates for the shortcomings of imaging in the visible wavelengths. In the NIR region, including the NIR I region (700–900 nm) and the NIR II region (1000–1700 nm), the human body exhibits low absorption and no interference from biological tissues, showing its great potential for bioimaging. Compared with other NIR materials, AuNCs have the advantages of simple preparation, high biocompatibility, easy surface modification, significant Stokes shifts and rapid elimination (Gong et al., 2021a). Therefore, modulation of the FL emission wavelength of AuNCs has been a hot research topic, and selecting suitable ligands for modification is one of the most commonly used strategies, such as proteins, polymers, and peptides (Figure 4) (Kumar and Tseng, 2020; Wu et al., 2010).

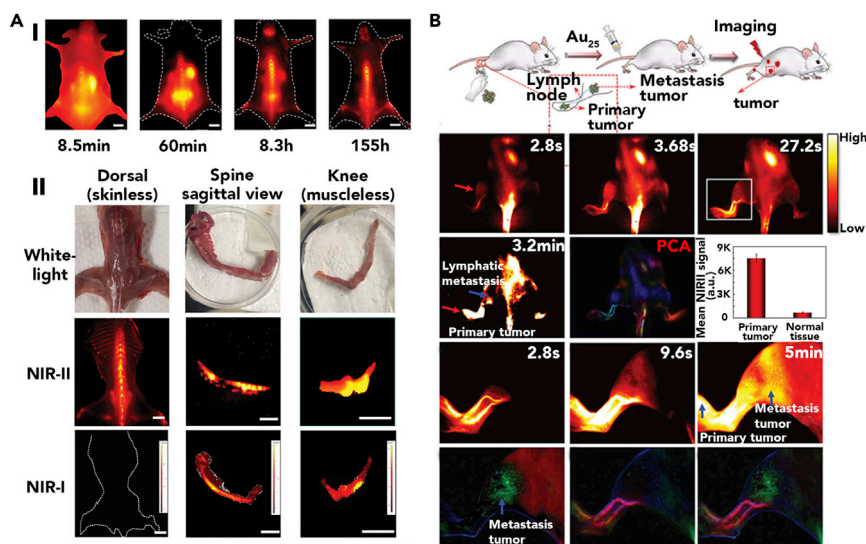


Figure 5. NIR-II imaging for potential FL-guided surgery

(A) (I) Whole-body NIR-II FL imaging of C57BL/6 mice after intravenous injection of AuNCs at different time points. (II) Ex vivo white light imaging, NIR-II FL imaging, and NIR-I FL imaging of the back, spine, and knee regions of C57BL/6 mice acquired 12 h after intravenous injection of AuNCs. Bar: 10 mm. Reproduced from Ref. (Li et al., 2020a), Copyright (2020), with permission of John Wiley and Sons.

(B) Imaging results of cage-like structures of Au₂₅(GSH)₁₈ in the NIR-II on tumor metastasis. Combined with PCA analysis, dynamic metastasis of the left leg tumor is shown. Green indicates tumor tissue, and red indicates blood vessels. Reproduced from Ref. (Liu et al., 2019), Copyright (2019), with permission of John Wiley and Sons.

GSH-AuNCs are the most studied fluorescent AuNCs with FL emission wavelengths, mainly in the visible range. Sun et al. (2017) used microwave heating time to prepare GSH-AuNCs with emission wavelengths up to 800 nm. The FL intensity of GSH-AuNCs shows a reversible linear temperature response. Adding FA to GSH-AuNCs has no effect on the FL emission peak, but it does allow GSH-AuNCs to target tumor cells for imaging. Au₂₅(SR)₁₈, the most studied AuNCs structure, has shown good dispersion and stability in many studies. Under 808-nanometer excitation, Li et al. (2020a) produced GSH-stabilized Au₂₅(GSH)₁₈ with FL emission of 1050 nm. Au₂₅(GSH)₁₈ binds efficiently to hydroxyapatite (HA, the main component of bone), showing concentration-dependent properties. This efficient binding is attributed to the specific binding of Au₂₅(GSH)₁₈ to Ca in HA, which is caused by the carboxyl group at the end of the GSH ligand on the Au₂₅(GSH)₁₈ surface. Within 8.5 min after Au₂₅(GSH)₁₈ injection, the whole mouse body exhibited a vital NIR-II FL. As the time was prolonged, Au₂₅(GSH)₁₈ was drastically reduced. Its signal was attenuated in other body parts but was enhanced in skeletal sites. After 8.3 h of injection, most mouse bones showed clear FL of the skeleton under the skin. When the skin was pulled away, almost all skeletal structures were photographed in high quality. This nanomaterial for direct observation of bone has great potential for guiding skeletal surgery and is an excellent NIR-II bone imaging probe (Figure 5A). Liu et al. (2019) created an Au₂₅(GSH)₁₈ cage structure with a red-shifted FL emission center at 1120 nm. Its surface ligand is altered by doping with metal atoms. The quantum yield of Au₂₅(GSH)₁₈ was increased by altering the electron transfer between the surface ligand and the metal nucleus by doping with metal atoms, which allowed penetration into the skull for NIR-II cerebrovascular imaging. Using principal component analysis techniques, primary tumors can also be clearly distinguished from tumor metastases (Figure 5B). When AuNCs are combined with Pt-based therapeutic agents, Pt transport can be observed by NIR-II imaging, allowing visualization of the tumor treatment process (Yang et al., 2020b). These AuNCs can also remove intracellular GSH, thus improving the therapeutic effect.

The diversity of ligands modified on the AuNCs surface offers several possibilities for NIR-II FL imaging. pH-sensitive AuNCs protected by α -lipoic acid (LA) and γ -cyclodextrin (γ -CD) were designed by Das et al. (2016). In an acidic environment, LA on the surface of AuNCs was converted to DHLA, leading to structural disruption. This eventually leads to efflux of-CD, which allows selective imaging of MCF7 human breast cancer cells. Tang et al. (2021) achieved high-resolution NIR-II imaging using BSA-protected AuNCs with the good photodynamic treatment of 4T1 breast cancer with an FL emission center of 1025 nm. Song et al. (2021)

developed CD-stabilized AuNCs with a 1050 nm FL emission center of CD-stabilized AuNCs. Wang et al. (2020) built a protein corona structure consisting of ribonuclease-A (RNase-A) on the surface of AuNCs with an FL emission wavelength of 1050 nm for gastrointestinal imaging and early tumor identification. Compared to rare earth and silver-based NIR-II emitters, RNase-A@AuNCs were more sensitive to the gastrointestinal tract, allowing precise examination of intestinal tumor nodules as small as 2.5 mm. NIR-II imaging with RNase-A@AuNCs was provided four times with a higher resolution of the gastrointestinal tract than the barium swallow method. Using AuNCs as a model, Er³⁺-doped rare earth (Ln) nanoparticles were further assembled, which significantly enhanced the PL intensity of AuNCs and could emit double the NIR-II luminescence under a single laser excitation, located at 1100 and 1550 nm, respectively (Li et al., 2022). The ratio of H₂S generation in NIR-II-targeted monitoring. AuNCs modified with short dithiol peptide chains (AuMHA/TDT, MHA: 6-mercaptohexanoic acid, TDT: terminal deoxynucleotidyl transferase) have a detection wavelength of 1250 nm and a high quantum yield (approximately 6%), allowing high-resolution imaging of whole-body blood arteries in mice (Yu et al., 2020). AuNCs with various functional components stabilized by peptides has also been created (Xia et al., 2018).

To provide an excellent combinatorial strategy for the multi-functionalization of AuNCs, researchers have used polyethylene glycol (PEG) to increase blood circulation time, matrix metalloproteinase (MMP)-2 peptides (CPLGVRGDs) to induce tumor targeting ability, *cis*-nicotinic anhydride modified doxorubicin to control drug release, and the photosensitizer e6 chloride (Ce6) to provide photodynamic therapy for photodynamic therapy. The AuNCs-LHRHa nanosystems were synthesized by combining luteinizing hormone releasing hormone analogs (LHRHa) with AuNCs, and LHRHa was used to enhance the uptake of nanosystems by tumor cells and improve the targeted imaging and photothermal therapy of prostate cancer (Wang et al., 2022). Using Keratin-modified AuNCs (AuNCs@Keratin) as a template, Li et al. (2020b) further synthesized silver ion-modified AuNCs@Keratin (AuNCsAg@Keratin) and gadolinium-induced AuNCs-Ag@Keratin (AuNCs-Ag@Keratin-Gd). Among them, the NIR FL intensity of AuNCs-Ag@Keratin-Gd was enhanced by 6.5 times compared with that of AuNCs@Keratin because silver modification promoted the formation of dense aggregates after gadolinium ion-induced assembly. In addition, because of gadolinium ion induction, AuNCs-Ag@Keratin-Gd can also achieve MR imaging, and it can be used as a drug carrier loaded with doxorubicin hydrochloride (DOX), which significantly inhibits tumor growth. Yang et al. (2020a) reported three α -lactalbumin-stabilized AuNCs, under the same exciter, had different emission spectra of 450, 520, and 705 nm (named AuNCs₄₅₀, AuNCs₅₂₀, and AuNCs₇₀₅, respectively). The emission wavelengths of the three clusters were pH dependent and intensity dependent on α -LA concentration, with AuNCs₇₀₅ having superior *in vivo* imaging signal-to-noise ratio and radiation efficiency for multimodal imaging and guiding surgical resection of breast tumors. These research results are expected to promote the multi-functionalization of AuNCs nanoprobe, stimulate the rational design of nanodrugs, and promote the development of *in vivo* bioimaging for multiple applications, laying the foundation for the integration of diagnosis and treatment.

Two-photon near-infrared fluorescence (TP-NIR-FL) imaging

Two-photon excitation of AuNCs is typically in the red to the near-infrared range, allowing them to penetrate deeply into the tissue. In addition, TPA occurs only in the focal plane, improving the spatial resolution (Figure 6). Jiang et al. (2019) used etching to create zwitterionic ligands (ZW) and 11-mercaptodecanoic acid (MUA)-stabilized AuNCs with excellent stability, resistance to photobleaching, and a large TPA cross-section (2.27×10^5 GM). By binding streptavidin and biotin alkyl ligands to AuNCs, the two clusters bioassembled intracellularly, amplified the firing signal, and successfully resisted quenching caused by AuNCs aggregation. Gong et al. (2021b) developed rhodamine B derivative-modified AuNCs that can be used as TP ratio fluorescent probes for real-time sensing and imaging of NO in neurons in brain regions. He et al. (2021) synthesized transferrin-modified AuNCs, which can emit TP near-infrared FL. They combined AuNCs with MnO₂ nanosheets to prepare a novel TP nanoprobe. The probe has a tissue penetration depth of 300 μ m, much larger than previously reported TP probes (<200 μ m). The probe can monitor the dynamic changes of endogenous GSH in living cells and tissues and enable dual TP-NIR FL and MIR imaging. Han et al. (2020b) prepared DHLA-modified AuNCs by etching, which has an ultra-high TPA cross section ($\sim 10^6$ GM) for TP imaging and can efficiently generate ROS, which, in combination with photodynamic therapy, exhibits superior antitumor effects.

Time-gated imaging with background and signal management based on TP imaging can improve the signal-to-noise ratio while reducing the impact of auto-fluorescence on image quality. Tian et al. (2021) created AuNCs stabilized by DHLA and conjugated galactosamine that are particularly capable of

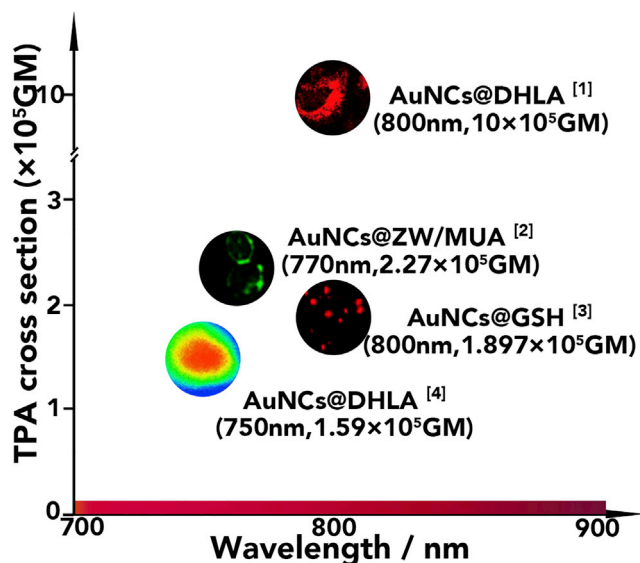


Figure 6. Two-photon near-infrared FL images of AuNCs with two-photon absorption cross-section up to $10 \times 10^5 \text{GM}$

[1] Adapted from Ref. (Han et al., 2020), Copyright (2020), with permission of American Chemical Society. [2] Adapted from Ref. (Jiang et al., 2019), Copyright (2019), with permission of American Chemical Society. [3] Adapted from Ref. (Polavarapu et al., 2011), Copyright (2009), with permission of Royal Society of Chemistry. [4] Adapted from Ref. (Tian et al., 2021), Copyright © 2021, Tian et al.

detecting liver cancer cells. The clusters have a long FL lifetime ($>300 \text{ ns}$) and significant TPA (TPA cross section up to $1.59 \times 10^5 \text{GM}$). Using an 800 nm laser for TP and TP time-gated imaging, the cluster could significantly remove the auto-fluorescence signal from the tissue, allowing real-time imaging of the liver and tumor.

Computed tomography (CT) imaging

CT is currently the most widely used medical diagnostic method. In clinical practice, high atomic number I-based compounds are often utilized as contrast agents to increase the contrast of CT scan sites (Hallouard et al., 2010). On the other hand, I-based contrast agents can produce allergic reactions, kidney damage, and short imaging times. These side effects severely limit their use in medical imaging. According to the X-ray absorption coefficient law, Au has a good X-ray absorption capacity because of its high density and atomic number. Au-based nanoparticles have attracted much attention as CT contrast agents due to their biocompatibility and modifiability (Figure 7). Because of their superior X-ray attenuation qualities, Hainfeld et al. (2006) pioneered the use of AuNPs as CT contrast agents with less interference to tissue imaging and longer imaging times. The results demonstrated the great potential of AuNPs as CT contrast agents, as they showed significantly higher CT attenuation than type I contrast agents of the same molar concentrations. Similarly, AuNCs are considered promising CT contrast agents. BSA-stabilized AuNCs have been shown to have higher CT values (Hounsfield units, HU) compared to type I contrast agents of the same concentration, with low BSA-AuNCs having HU values comparable to those of high concentrations of iopromide (Wang et al., 2015c; Zhang et al., 2012a). Since BSA-AuNCs are mainly excreted in the kidney, details of the renal tissue can be observed, and renal lesions can be diagnosed (Figure 8A). In addition to dual-mode imaging by combining FL and CT, the FL properties of AuNCs can enhance tumor accumulation and enable tumor radiotherapy (Zhang et al., 2013, 2014; Zheng et al., 2021b).

The ability of AuNCs to perform CT imaging can be improved by adding different functional auxiliary complexes to their surfaces. Guo et al. (2010) created dendrimer-encapsulated AuNCs (AuDENPs) using a fifth-generation polyamidoamine (G5 PAMAM) dendrimer as a template. They altered AuDENPs by surface PEGylation and acetylation to circumvent the toxicity and non-specificity of surface amino groups (Peng et al., 2011, 2012). All modified AuDENPs outperformed type I contrast agents in imaging contrast, circulation time, and local enrichment because of the effects of electron paramagnetic resonance (EPR) and lack of comparable cytotoxicity. AS1411 aptamer-modified AuNPs (AS1411-DA-AuNPs) targeted ditriazoic acid

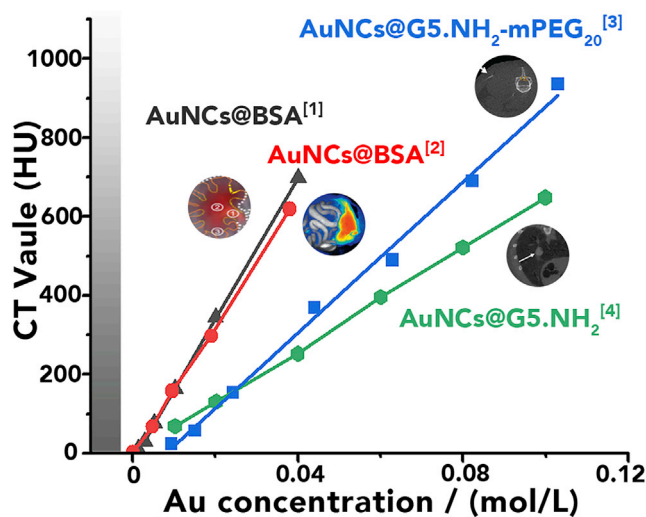


Figure 7. The HU values of the different AuNCs and as a function of the Au concentrations

[1] Adapted from Ref. (Wang et al., 2015c), Copyright (2015), with permission of American Chemical Society. [2] Adapted from Ref. (Zhang et al., 2012a), Copyright (2012), with permission of Elsevier. [3] Adapted from Ref. (Guo et al., 2010), Copyright (2010), with permission of American Chemical Society. [4] Adapted from Ref. (Peng et al., 2012), Copyright (2012), with permission of Elsevier.

and nucleolin to localize CL1-5 tumor sites accurately (Li et al., 2015). Both I and Au contribute to high X-ray absorption coefficients and strong CT signals (Chen et al., 2017; Clark et al., 2013). They allow simultaneous FL and CT imaging to guide tumor resection. NPs composed of Au and I can also diagnose thyroid cancer and image tumor vasculature. Zhou et al. (2013) designed a silica-coated FA-modified AuNCs targeting FR (+) MGC803 and FR (-) GES-1 cells for dual-mode imaging of FL and CT in gastric cancer (Figure 8B). Chu et al. (2019) in BSA-AuNCs introduced Ag⁺ and found that a molar ratio of Au: Ag of 3:2 showcased the best X-ray attenuation coefficient, approximately twice that of iohexol (80 mM concentration). This compound can be used as a potential CT contrast agent. Similarly, the complex of Fe²⁺ with AuNCs improves CT imaging, and the presence of Fe²⁺ allows MRI, thus laying the foundation for multimodal imaging (Zhao et al., 2016a). AuroVist™ is a commercially available nano Au X-ray contrast agent with a size of 1.9 nm (Clark et al., 2013). It exhibits the following characteristics: high imaging contrast, which is three times higher than that of type I contrast agents; low toxicity, which is more than four times the concentration of type I contrast agents; and long retention time, which the kidneys can clear.

Positron emission tomography (PET) imaging

PET imaging allows imaging at the cellular and molecular levels, making it one of the most advanced diagnostic medical imaging techniques available. Living metabolites are labeled with short-lived radionuclides, and their aggregation in human metabolism can reflect the living metabolism (Ziegler, 2005). Currently, PET is widely used for diagnosing and treating cancer, coronary heart disease, and brain diseases (Burgess et al., 2001; Delbeke and Martin, 2001; Hagge et al., 2001; Machac, 2005). PET imaging agents are typically glucose analogues, such as ¹⁸F-FDG, which are based on glucose metabolism and cause massive ¹⁸F-FDG aggregation at tumor locations (Duysinx et al., 2004). This non-specific tracer makes diagnosis and prognosis more difficult because it cannot target the tumor locations. In addition, the poor stability of commonly used radionuclides hinders PET imaging studies. Directly doping radionuclides into AuNCs can significantly improve their stability and sensitivity detection. The commonly used radionuclides are ⁶⁴Cu, ⁶⁸Ga, and ¹²⁴I (Ballegeer et al., 2013; Cho et al., 2015; Petersen et al., 2011; Wu et al., 2019).

Zhao et al. (2014a) prepared ⁶⁴CuAuNPs with diameters of 9.4 ± 1.2 nm by directly doping ⁶⁴Cu into the lattice of AuNPs in an alloyed manner. The NPs showed good radionuclide labeling stability with no degradation in mouse serum for 48 h. The NP retention was high in liver and kidney sites. Therefore, they further reduced the size of ⁶⁴CuAuNPs to 2.5 ± 0.8 nm and PEGylated the surface of ⁶⁴CuAuNCs, improving the biosafety and enhancing the renal clearance of NCs (Zhao et al., 2014b). However, the AuNCs made this way were non-specific, and their distribution was not uniform in targeting and identifying specific

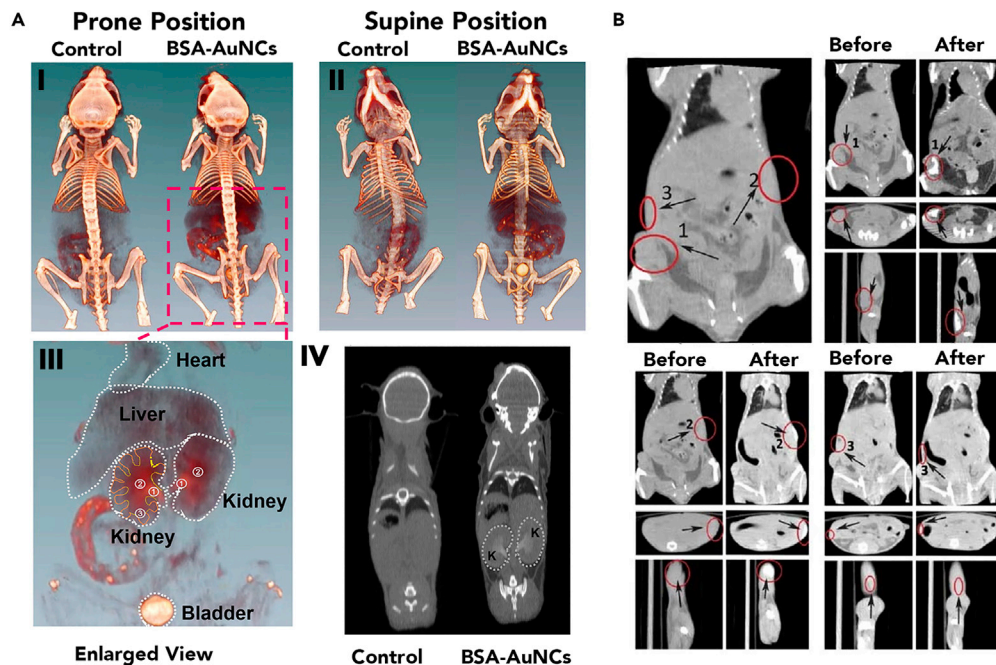


Figure 8. CT imaging

(A) (I, II) *In vivo* 3D CT images of mice injected with saline and BSA-AuNCs in (a) prone (b) supine positions and 2 h after injection. (III) Magnified view of the major organs of BSA-AuNCs injected mice. (IV) *In vivo* 2D CT images of saline (left) and BSA-AuNCs injected (right) mice at 2 h post-injection. Adapted from Ref. (Wang et al., 2015c), Copyright (2015), with permission of American Chemical Society.

(B) Comparative CT imaging of three different sites before and after injection of FA-AuNCs@SiO₂ in a nude mouse model of gastric cancer. Red circle 1 shows the tumor site, red circle 2 shows the dorsal injection site, and red circle 3 shows the uninjected control group (Zhou et al., 2013). Copyright © 2013, Zhou et al.

tumors. Zhao et al. (2016b) modified ⁶⁴CuAuNCs using AMD3100 to achieve high sensitivity and accuracy in detecting C-X-C chemokine receptor 4 (CXCR4) expression (Figure 9A). In a mouse model of breast cancer, these clusters can target and identify tumor sites and show better PET imaging of tumor metastases, especially lung metastases. ⁶⁴Cu-AuNCs-ECL1i (ECL1i: extracellular loop 1 inverso peptide) was synthesized by conjugating chemokine (C-C Motif) receptor 2 (CCR2) to ⁶⁴CuAuNCs to specifically identify triple-negative breast cancer and improve tumor and contrast of background PET imaging (Figure 9B) (Zhao et al., 2021). This receptor is also highly expressed in cells with atherosclerotic lesions. In an ApoE^{-/-} mouse model with progressive atherosclerosis, ⁶⁴Cu-AuNCs-ECL1i is sensitive to early lesions and shows dynamic changes in lesions, indicating its great potential for detecting and imaging atherosclerotic disease (Sultan et al., 2021).

Several researchers labeled AuNCs with ⁶⁸Ga, ¹²⁴I for PET-CT imaging. Han et al. (2020a) labeled human serum albumin and luteinizing hormone-releasing hormone-modified AuNCs with ¹²⁴I and achieved a 73% labeling rate for targeted identification of tumor tissue in the lungs. Zheng et al. (2021a) prepared two types of ⁶⁸Ga-labeled AuNCs, namely GSH-AuNCs (⁶⁸Ga-GSH@AuNCs) and GSH and arginine-glycine-aspartate tripeptide (RGD) co-modified AuNCs (⁶⁸Ga-RGD-GSH@AuNCs). ⁶⁸Ga-RGD-GSH@AuNCs have a shorter distribution half-life and longer elimination half-life, allowing them to rapidly enter the tumor site and provide a longer blood circulation time. Compared with ⁶⁸Ga-GSH@AuNCs, ⁶⁸Ga-RGD-GSH@AuNCs can specifically identify tumor sites, exhibit more pronounced aggregation at tumor sites and play a more significant role in early tumor PET-CT imaging and detection due to the presence of RGD. However, due to the high affinity of RGD for renal tubules, ⁶⁸Ga-RGD-GSH@AuNCs also aggregated mainly in the kidney.

Magnetic resonance imaging (MRI)

MRI uses the resonance of atomic nuclei in a magnetic field to reconstruct images. This method determines the spatial distribution of the H⁺ density and its relaxation time in human tissues (Huk and Gademann, 1984). Since it

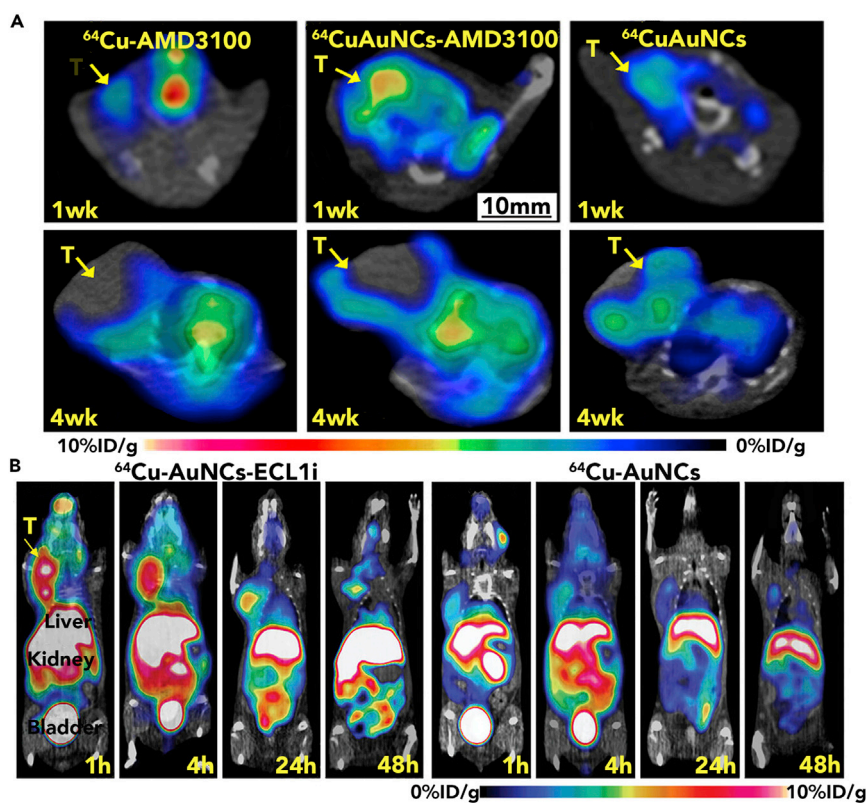


Figure 9. PET imaging

(A) Cumulative PET/CT images comparing contrast agents in lung tumors at week 1 and week 4 after injection of ^{64}Cu -AMD3100, $^{64}\text{CuAuNCs-AMD3100}$, and $^{64}\text{Cu-AuNCs}$ into 4T1 tumor-bearing mice, respectively. Reproduced from Ref. (Zhao et al., 2016b), Copyright (2016), with permission of American Chemical Society.

(B) PET/CT images of $^{64}\text{Cu-AuNCs-ECL1i}$ versus $^{64}\text{Cu-AuNCs}$ at different times after injection into a 4T1 tumor-bearing mouse model. Adapted from Ref. (Zhao et al., 2021), Copyright (2021), with permission of John Wiley and Sons.

utilizes the hydrogen nucleus of water in the body, there is no danger of ionizing radiation. MRI provides images with high spatial resolution and excellent tissue information without radiation, thus offering advantages in diagnosing diseases. Although MRI has long been used for clinical diagnosis, its low sensitivity limits its usefulness. Thus, MRI contrast agents play a crucial role in enhancing image contrast by significantly altering the differences in physicochemical quality of nearby tissues (Aime et al., 2006; Na et al., 2009).

Gd^{3+} complexes, such as Gd-DTPA (DTPA: Diethylenetriaminepentaacetic acid) and Gd-EOB-DTPA (EOB: gadolinium ethoxybenzyl), are currently used as MRI contrast agents (Tamada et al., 2009; Werner et al., 2008). However, the low tumor targeting, high renal clearance and toxic side effects of Gd^{3+} complexes severely limit their use. Coupling of AuNCs with Gd^{3+} complexes is a novel approach to developing MRI contrast agents (Figure 10). The FL properties of AuNCs enable AuNCs probes to be optically imaged, and the combination of multiple imaging modalities can guide subsequent treatment more effectively. MR and FL imaging probes were prepared by covalently grafting Gd-DTPA on BSA-stabilized AuNCs. These probes showed significantly higher Gd^{3+} relaxation rates, five times higher than clinical Gd-DTPA while maintaining the FL intensity of AuNCs (Sun et al., 2013). Han et al. (2017) prepared nanocrystals of Gd_2O_3 based on a BSA biomineralization method and constructed a new therapeutic platform by combining them with AuNCs. The platform was loaded with indocyanine green (ICG) for NIRF/MR/CT triple-mode imaging, which allowed simultaneous photothermal and photodynamic therapy due to the absorption of ICG in the NIR range. The relaxation rates of Gd-AuNCs generated in one step by biomineralization were slightly higher than those of the probes as mentioned above, implying that the properties of the clusters were modified by the synthesis process (Le et al., 2016; Liang and Xiao, 2017). Liang and Xiao (2017) investigated the effect of the production process on the optical and chiral characteristics of nanoprobe using BSA and Lys as protein models (Liang and Xiao, 2017). The results showed that AuNCs templated by proteins were first constructed to bind directly to DTPA with higher purity and

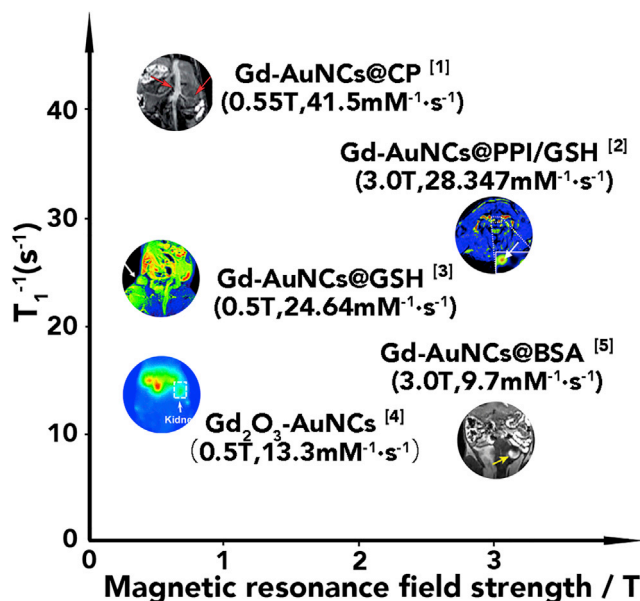


Figure 10. Longitudinal (T_1) relaxation times and magnetic resonance field strengths of AuNCs complexed with Gd^{3+} as MRI contrast agents

[1] Adapted from Ref. (Liang et al., 2013), Copyright (2013), with permission of Royal Society of Chemistry. [2] Adapted from Ref. (Wang et al., 2019), Copyright (2019), with permission of Elsevier. [3] Adapted from Ref. (Hou et al., 2017), Copyright (2016), with permission of Elsevier. [4] Adapted from Ref. (Han et al., 2017), Copyright (2017), with permission of American Chemical Society. [5] Adapted from Ref. (Liang and Xiao, 2017), Copyright (2013), with permission of Royal Society of Chemistry.

relaxation rates. Compared to BSA-AuNCs, Lys-AuNCs are smaller, exhibit a larger Gd: AuNCs ratio, and show better MR images when using commercial Gd-DTPA probes (Figure 11A) (Hou et al., 2017). Gd^{3+} and the negatively charged carboxyl groups of AuNCs can also self-assemble AuNCs into monodisperse spherical particles (GNCNs) through electrostatic interactions, enhancing the PL of AuNCs. Because of the EPR effect, GNCNs aggregated at the tumor site and showed a high MR signal within 60 min, resulting in a significant increase in the brightness of the tumor site. Wang et al. (2019) covalently linked the scavenger receptor (SRAI)-specific peptide pp1 to Gd-AuNCs to target atherosclerotic plaques and enhance plaque contrast (Figure 11B).

Bonnet et al. (2009) combined a cyclic dodecapeptide (CP) with Gd^{3+} , which showed excellent relaxation times. Following this work, altered the complex by replacing three amino acid residues on the CP backbone with tyrosine and two cysteine residues, producing a novel CP that was used to create CP-AuNCs (Liang et al., 2013). When $GdCl_3$ was added to CP-AuNCs, Gd^{3+} adsorbed on the surface of AuNCs via CP to generate Gd-AuNCs, dramatically increasing the chirality of the Gd^{3+} complex by 10-fold compared to Gd-DTPA and prolonged the intravascular circulation of Gd^{3+} . The addition of Gd^{3+} did not affect the size of AuNCs, and their tiny size distribution allowed them to be excreted via urine.

The binding of Fe complexes to AuNCs also yielded good MRI contrast agents. Zhao et al. (2016a) synthesized Fe^{2+} -complexed AuNCs *in situ* at tumor sites, and the presence of Fe^{2+} enabled MRI. Wang et al. (2015a) prepared hydrophilic iron oxide NPs via electrostatic adsorption on AuNCs as nano-bioimaging probes ($Fe_3O_4@AuNCs$) with red FL for MR/FL imaging. Fe_3O_4 NPs can increase the transverse relaxation rate to $20.4 mM^{-1} S^{-1}$. Experimental results show that the contrast of MR images decreases as the concentration of $Fe_3O_4@AuNCs$ increases. Achieving good imaging with a low concentration of contrast agents would significantly reduce the burden on the patient's body.

Photoacoustic (PA) imaging

Imaging is a new biomedical imaging approach based on laser ultrasound that has been developed in recent years. High imaging resolution, low acoustic attenuation, and significant tissue penetration depth (about 10 cm) are all advantages of PA imaging (Wang and Hu, 2012; Wang and Yao, 2016). In addition, the non-invasive and

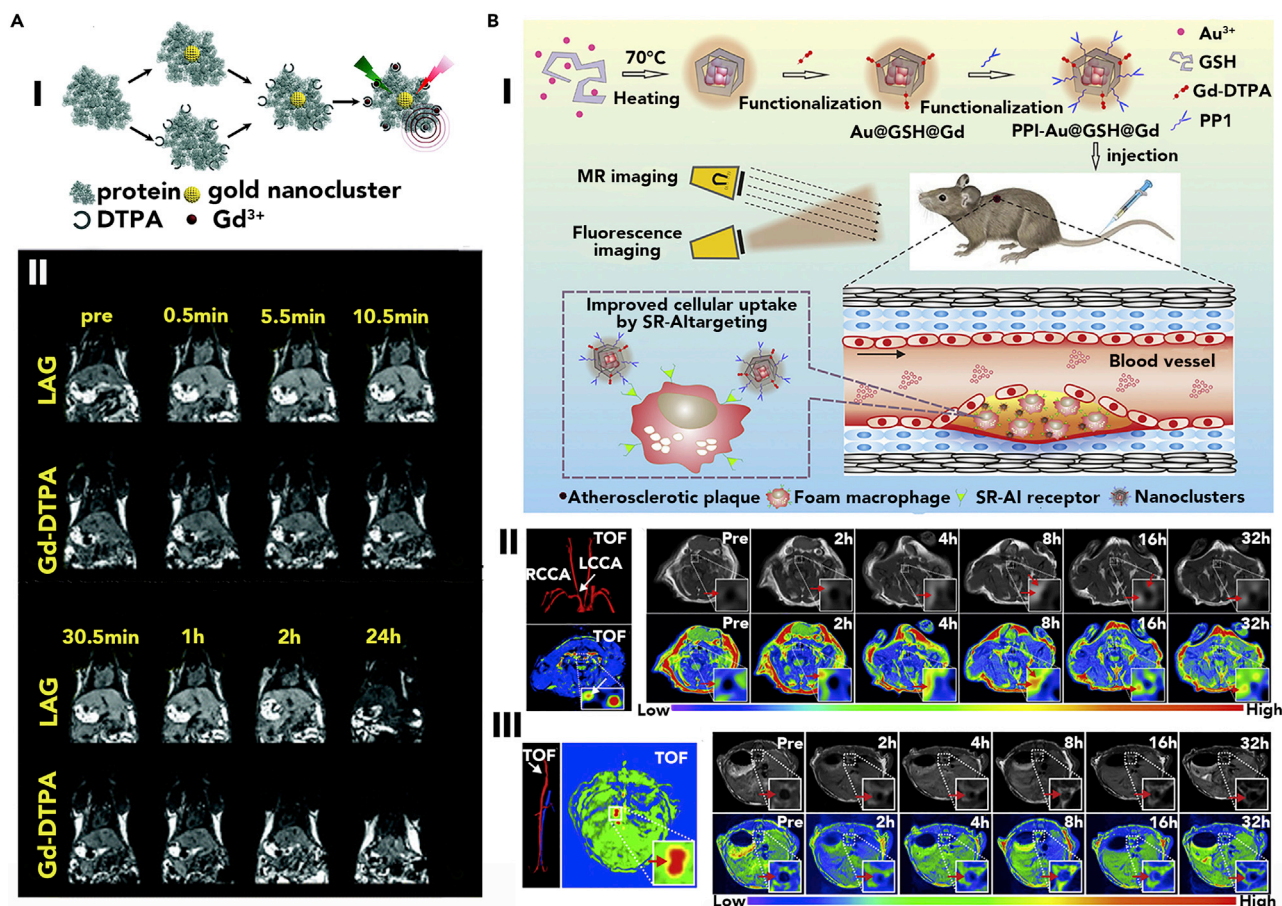


Figure 11. MR imaging

(A) (I) Schematic diagram of two synthetic routes for the preparation of gold nanoclusters using a protein model. (II) T1-weighted images of Kunming mice at different times after intravenous injection of LAG (0.00768mmolGd/kg) or Gd-DTPA (0.02mmolGd/kg). Reproduced from Ref. (Liang and Xiao, 2017), Copyright (2017), with permission of Royal Society of Chemistry.

(B) (I) Schematic diagram of PP1-Au@GSH@Gd-NCs dual-modal imaging probe for atherosclerotic plaque MR/FL imaging. (II, III) T1-weighted images of signal changes over time in plaques at the right common carotid artery and aorta of mice injected with PP1-Au@GSH@Gd-NCs. Arrows indicate the location of the increased signal within the plaque. Reproduced from Ref. (Wang et al., 2019), Copyright (2019), with permission of Elsevier.

non-ionizing nature of PA imaging ensures its safety and reproducibility. Endogenous chromophores (oxyhemoglobin, deoxyhemoglobin, melanin, lipids, and collagen) are used as imaging molecules in PA imaging and exogenous contrast agents with solid light absorption properties (fluorescent moieties, precious metal NPs, carbon-based nanomaterials, polymers, and other inorganic materials) (Upputuri and Pramanik, 2020). Exogenous contrast agents are used to improving the resolution and signal-to-noise ratio of PA imaging and to achieve directional imaging. AuNPs exhibiting surface plasmon resonance effects and NIR absorption have attracted much attention as exogenous contrast agents (Li and Chen, 2015). AuNPs commonly used for PA imaging include Au nanorods, Au nanoflowers, Au nanocages, vesicles, and oversized spherical AuNPs (>5 nm in diameter) (Chen et al., 2021; Huang et al., 2013; Santos et al., 2021; Wang et al., 2021; Yan et al., 2021).

AuNCs have also been used for PA imaging. Gao et al. (2018) prepared BSA-AuNCs with a particle size of approximately 3 nm as a contrast agent for dual-mode imaging of FL and PA. The imaging capability of the clusters was verified in an adult zebrafish model. AuNCs with ICG were more effective in PA imaging (Higbee-Dempsey et al., 2019). In addition, AuNCs-ICG nanoprobes (AuNCs-INPs), synthesized with AuNCs components conjugated to ICG, can be used not only for NIRF and PA imaging but also for real-time monitoring of tumor therapy (Figure 12) (Cui et al., 2017). Compared to ICG, The PA intensity of AuNCs are more intense and significantly increase in intensity with increasing ICG concentration. This probe enhances the accumulation of ICG at the tumor site and prolongs the residence time of ICG, allowing it to be used for targeted tumor

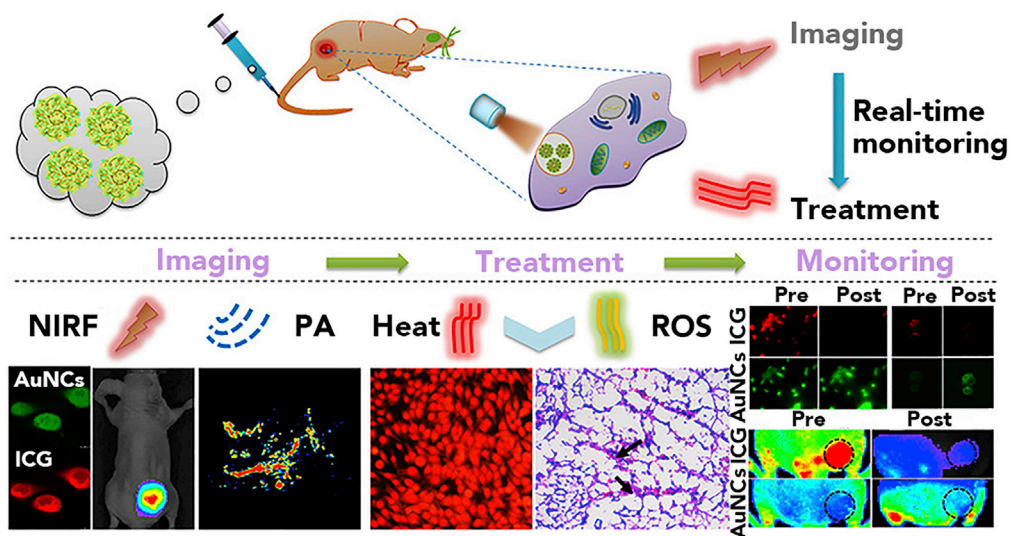


Figure 12. PA imaging

Schematic diagram of ICG-AuNCs for imaging, treatment monitoring integration. Reproduced from Ref. (Cui et al., 2017), Copyright (2017), with permission of American Chemical Society.

therapy. Photoacoustic signals were better in AuNCs stabilized by zwitterionic ligands (Shen et al., 2017). Ning et al. (2017) produced AuNPs of various sizes (2.5–6 nm) and investigated the effect of AuNP size and ligand ratio on FL and PA signals. The number of ligands decreases with increasing Au:Zw ratio, which increases the size of Au nuclei. As a result, more heat and more powerful vibrations are generated under light irradiation, increasing the intensity of the PA signal. At the same time, non-radiative losses rise, FL increases and intensity decreases. This finding suggests that the intensity of the PA signal is closely related to the size of the Au nucleus and the number of ligands. Therefore, future studies should focus on modulating the size of the Au nucleus and the coverage of ligands to provide optimal PA and FL imaging results.

SUMMARY AND OUTLOOK

This article presents the scientific progress of AuNCs in bioimaging applications in detail. By adjusting the synthesis method and selecting different ligands for modification, the prepared AuNCs can show tunable FL from the visible to near-infrared region, allowing them to be employed as fluorescent probes for visible and near-infrared wavelengths. Because of their high atomic number and electron density, AuNCs can also be used as contrast agents for CT and PA imaging. The FL properties of AuNCs can be modified by doping the backbone with metals (such as ^{64}Cu , ^{68}Ga , ^{124}I , Ga^{3+}) and can be used for PET and MR imaging. Because the modification is easy, AuNCs with various ligand alterations can be produced, allowing the creation of imaging probes with many advantages.

Medical research relied on early and precise disease diagnosis and targeted therapy, and the superior physicochemical qualities and biocompatibility of AuNCs make them a particularly intriguing material choice. Despite the tremendous progress made in recent years, many difficulties still need to be addressed before AuNCs may be widely used.

First, most AuNCs currently produced have a low quantum yield, which reduces the detection sensitivity and also affects the detection limit. Second, despite the remarkable biocompatibility of AuNCs, studies on AuNCs imaging have so far included only cellular and animal tests, with no application in humans. Extensive studies on the metabolism, tissue distribution and toxicity of AuNCs are needed for *in vivo* imaging in humans.

Finally, each imaging modality has its own set of restrictions. Developing nanomaterials that combine multiple imaging modalities to enable nanoplateforms with high sensitivity, real-time, and precise localization of anatomical components could improve disease detection and treatment. Although AuNCs probes have been used in certain multimodal imaging studies, these studies are still in their early stages and need to be further explored.

ACKNOWLEDGMENTS

The work was supported by the National Natural Science Foundation of China (52273110, 21975191, 21805218, 51873168), the Natural Science Foundation of Hubei Province (2021CFB299, 2021CFB301), Knowledge Innovation Program of Wuhan-Shuguang Project [20221j0044], Fundamental Research Funds for the Central Universities (WUT) [2021III035JC, 2020III009GX, 2020III035GX], and State Key Laboratory of Advanced Technology for Materials Synthesis and Processing (WUT) [Grant number 2022-KF-27].

AUTHOR CONTRIBUTIONS

Conceptualization: G.G. and S.T.; investigation: Z.C., G.X. and G.G.; visualization: Z.C., G.X. and G.G.; funding acquisition: G.G., H.M. and S.T.; project administration: G.G.; supervision: G.G. and S.T.; writing-original draft: Z.C., G.X. and G.G.; writing-review & editing: C.W., H.M., Y.Y. and G.G.

DECLARATION OF INTERESTS

The authors declare that they have no competing interests.

REFERENCES

- Abbas, M.A., Kamat, P.V., and Bang, J.H. (2018). Thiolated gold nanoclusters for light energy conversion. *ACS Energy Lett.* 3, 840–854. <https://doi.org/10.1021/acsenerylett.8b00070>.
- Agrachev, M., Antonello, S., Dainese, T., Ruzzi, M., Zoleo, A., Aprà, E., Govind, N., Fortunelli, A., Sementa, L., and Maran, F. (2017). Magnetic ordering in gold nanoclusters. *ACS Omega* 2, 2607–2617. <https://doi.org/10.1021/acsomega.7b00472>.
- Aime, S., Crich, S.G., Gianolio, E., Giovenzana, G.B., Tei, L., and Terreno, E. (2006). High sensitivity lanthanide(III) based probes for MR-medical imaging. *Coord. Chem. Rev.* 250, 1562–1579. <https://doi.org/10.1016/j.ccr.2006.03.015>.
- Alkan, F., Pandeya, P., and Aikens, C.M. (2019). Understanding the effect of doping on energetics and electronic structure for Au₂₅, Ag₂₅, and Au₃₈ clusters. *J. Phys. Chem. C* 123, 9516–9527. <https://doi.org/10.1021/acs.jpcc.9b00065>.
- Alonso, M.C., Trapiella-Alfonso, L., Fernández, J.M.C., Pereiro, R., and Sanz-Medel, A. (2016). Functionalized gold nanoclusters as fluorescent labels for immunoassays: application to human serum immunoglobulin E determination. *Biosens. Bioelectron.* 77, 1055–1061. <https://doi.org/10.1016/j.bios.2015.08.011>.
- Alric, C., Miladi, I., Kryza, D., Taleb, J., Lux, F., Bazzi, R., Billotey, C., Janier, M., Perriat, P., Roux, S., and Tillement, O. (2013). The biodistribution of gold nanoparticles designed for renal clearance. *Nanoscale* 5, 5930–5939. <https://doi.org/10.1039/c3nr00012e>.
- Bai, Y., Shu, T., Su, L., and Zhang, X. (2020). Fluorescent gold nanoclusters for biosensor and bioimaging application. *Crystals* 10, 357. <https://doi.org/10.3390/cryst10050357>.
- Ballegeer, E.A., Madrill, N.J., Berger, K.L., Agnew, D.W., and McNiel, E.A. (2013). Evaluation of hypoxia in a feline model of head and neck cancer using ⁶⁴Cu-ATSM positron emission tomography/computed tomography. *BMC Cancer* 13, 218. <https://doi.org/10.1186/1471-2407-13-218>.
- Ballou, B., Ernst, L.A., and Waggoner, A.S. (2005). Fluorescence imaging of tumors *in vivo*. *Curr. Med. Chem.* 12, 795–805. <https://doi.org/10.2174/0929867053507324>.
- Bonnet, C.S., Fries, P.H., Crouzy, S., Sénèque, O., Cisnetti, F., Boturyn, D., Dumy, P., and Delangle, P. (2009). A gadolinium-binding cyclodecapeptide with a large high-field relaxivity involving second-sphere water. *Chemistry* 15, 7083–7093. <https://doi.org/10.1002/chem.200900636>.
- Brust, M., Walker, M., Bethell, D., Schiffrin, D.J., and Whyman, R. (1994). Synthesis of thiol-derivatized gold nanoparticles in a two-phase Liquid-Liquid system. *J. Chem. Soc. Chem. Commun.* 7, 801–802. <https://doi.org/10.1039/c39940000801>.
- Burgess, P.W., Quayle, A., and Frith, C.D. (2001). Brain regions involved in prospective memory as determined by positron emission tomography. *Neuropsychologia* 39, 545–555. [https://doi.org/10.1016/S0028-3932\(00\)00149-4](https://doi.org/10.1016/S0028-3932(00)00149-4).
- Chan, W.C., and Nie, S. (1998). Quantum dot bioconjugates for ultrasensitive nonisotopic detection. *Science* 281, 2016–2018. <https://doi.org/10.1126/science.281.5385.2016>.
- Chen, Y.S., Hung, Y.C., Liao, I., and Huang, G.S. (2009). Assessment of the *in vivo* toxicity of gold nanoparticles. *Nanoscale Res. Lett.* 4, 858–864. <https://doi.org/10.1007/s11671-009-9334-6>.
- Chen, F., Goel, S., Hernandez, R., Graves, S.A., Shi, S., Nickles, R.J., and Cai, W. (2016). Dynamic positron emission tomography imaging of renal clearable gold nanoparticles. *Small* 12, 2775–2782. <https://doi.org/10.1002/sml.201600194>.
- Chen, X., Zhu, H., Huang, X., Wang, P., Zhang, F., Li, W., Chen, G., and Chen, B. (2017). Novel iodinated gold nanoclusters for precise diagnosis of thyroid cancer. *Nanoscale* 9, 2219–2231. <https://doi.org/10.1039/c6nr07656d>.
- Chen, Y., Zhou, M., Li, Q., Gronlund, H., and Jin, R. (2020). Isomerization-induced enhancement of luminescence in Au₂₈(SR)₂₀ nanoclusters. *Chem. Sci.* 11, 8176–8183. <https://doi.org/10.1039/d0sc01270j>.
- Chen, Y., Xu, C., Cheng, Y., and Cheng, Q. (2021). Photostability enhancement of silica-coated gold nanostars for photoacoustic imaging guided photothermal therapy. *Photoacoustics* 23, 100284. <https://doi.org/10.1016/j.pacs.2021.100284>.
- Cho, B.-B., Park, J.H., Jung, S.J., Lee, J., Lee, J.H., Hur, M.G., Justin Raj, C., and Yu, K.-H. (2015). Synthesis and characterization of ⁶⁸Ga labeled Fe₃O₄ nanoparticles for positron emission tomography (PET) and magnetic resonance imaging (MRI). *J. Radioanal. Nucl. Chem.* 305, 169–178. <https://doi.org/10.1007/s10967-015-4026-4>.
- Choi, H.S., Liu, W., Misra, P., Tanaka, E., Zimmer, J.P., Iyiti Ipe, B., Bawendi, M.G., and Frangioni, J.V. (2007). Renal clearance of quantum dots. *Nat. Biotechnol.* 25, 1165–1170. <https://doi.org/10.1038/nbt1340>.
- Chu, Z., Chen, L., Wang, X., Yang, Q., Zhao, Q., Huang, C., Huang, Y., Yang, D.P., and Jia, N. (2019). Ultrasmall Au-Ag alloy nanoparticles: protein-directed synthesis, biocompatibility, and X-ray computed tomography imaging. *ACS Biomater. Sci. Eng.* 5, 1005–1015. <https://doi.org/10.1021/acsbomaterials.8b01176>.
- Clark, D.P., Ghaghada, K., Moding, E.J., Kirsch, D.G., and Badea, C.T. (2013). *In vivo* characterization of tumor vasculature using iodine and gold nanoparticles and dual energy micro-CT. *Phys. Med. Biol.* 58, 1683–1704. <https://doi.org/10.1088/0031-9155/58/6/1683>.
- Cong, Y., Wang, X., Zhu, S., Liu, L., and Li, L. (2021). Spiropyran-functionalized gold nanoclusters with photochromic ability for light-controlled fluorescence bioimaging. *ACS Appl. Bio Mater.* 4, 2790–2797. <https://doi.org/10.1021/acsbm.1c00011>.
- Cui, M., Zhao, Y., and Song, Q. (2014). Synthesis, optical properties and applications of ultra-small luminescent gold nanoclusters. *TrAC, Trends Anal. Chem.* 57, 73–82. <https://doi.org/10.1016/j.trac.2014.02.005>.
- Cui, H., Hu, D., Zhang, J., Gao, G., Chen, Z., Li, W., Gong, P., Sheng, Z., and Cai, L. (2017). Gold nanoclusters-indocyanine green nanoprobe for synchronous cancer imaging, treatment, and real-time monitoring based on fluorescence resonance energy transfer. *ACS Appl. Mater. Interfaces* 9, 25114–25127. <https://doi.org/10.1021/acsbm.7b06192>.

- Das, T., Poria, D.K., and Purkayastha, P. (2016). NIR-emitting chiral gold nanoclusters coated with gamma-cyclodextrin are pH sensitive: application as biomarker. *Nanomedicine* 12, 1105–1112. <https://doi.org/10.1016/j.nano.2015.12.386>.
- Delbeke, D., and Martin, W.H. (2001). Positron emission tomography imaging in oncology. *Radiol. Clin. North Am.* 39, 883–917. [https://doi.org/10.1016/S0033-8389\(05\)70319-5](https://doi.org/10.1016/S0033-8389(05)70319-5).
- Du, B., Jiang, X., Das, A., Zhou, Q., Yu, M., Jin, R., and Zheng, J. (2017). Glomerular barrier behaves as an atomically precise bandpass filter in a sub-nanometre regime. *Nat. Nanotechnol.* 12, 1096–1102. <https://doi.org/10.1038/nnano.2017.170>.
- Du, B., Yu, M., and Zheng, J. (2018). Transport and interactions of nanoparticles in the kidneys. *Nat. Rev. Mater.* 3, 358–374. <https://doi.org/10.1038/s41578-018-0038-3>.
- Duysinx, B., Nguyen, D., Louis, R., Cataldo, D., Belhocine, T., Bartsch, P., and Bury, T. (2004). Evaluation of pleural disease with 18-fluorodeoxyglucose positron emission tomography imaging. *Chest* 125, 489–493. <https://doi.org/10.1378/chest.125.2.489>.
- El-Sayed, N., and Schneider, M. (2020). Advances in biomedical and pharmaceutical applications of protein-stabilized gold nanoclusters. *J. Mater. Chem. B* 8, 8952–8971. <https://doi.org/10.1039/d0tb01610a>.
- Feng, B., Xing, Y., Lan, J., Su, Z., and Wang, F. (2020). Synthesis of MUC1 aptamer-stabilized gold nanoclusters for cell-specific imaging. *Talanta* 212, 120796. <https://doi.org/10.1016/j.talanta.2020.120796>.
- Fernando, A., and Aikens, C.M. (2015). Ligand exchange mechanism on thiolate monolayer protected Au₂₅(SR)₁₈ nanoclusters. *J. Phys. Chem. C* 119, 20179–20187. <https://doi.org/10.1021/acs.jpcc.5b06833>.
- Fu, Q., Zhu, R., Song, J., Yang, H., and Chen, X. (2019). Photoacoustic imaging: contrast agents and their biomedical applications. *Adv. Mater.* 31, e1805875. <https://doi.org/10.1002/adma.201805875>.
- Gan, Z., Lin, Y., Luo, L., Han, G., Liu, W., Liu, Z., Yao, C., Weng, L., Liao, L., Chen, J., et al. (2016). Fluorescent gold nanoclusters with interlocked staples and a fully thiolate-bound kernel. *Angew. Chem. Int. Ed. Engl.* 55, 11567–11571. <https://doi.org/10.1002/anie.201606661>.
- Gao, D., Liu, Y., Wang, Y., and Yuan, Z. (2018). Protein-modified ultra-small gold clusters for dual-modal *in vivo* fluorescence/photoacoustic imaging. *Quant. Imaging Med. Surg.* 8, 326–332. <https://doi.org/10.21037/qims.2018.03.01>.
- Gao, G., Chen, R., He, M., Li, J., Li, J., Wang, L., and Sun, T. (2019). Gold nanoclusters for Parkinson's disease treatment. *Biomaterials* 194, 36–46. <https://doi.org/10.1016/j.biomaterials.2018.12.013>.
- Gong, L., Shan, X., Zhao, X.H., Tang, L., and Zhang, X.B. (2021a). Activatable NIR-II fluorescent probes applied in biomedicine: progress and perspectives. *ChemMedChem* 16, 2426–2440. <https://doi.org/10.1002/cmdc.202100142>.
- Gong, Z., Liu, Z., Zhang, Z., Mei, Y., and Tian, Y. (2021b). A highly stable two-photon ratiometric fluorescence probe for real-time biosensing and imaging of nitric oxide in brain tissues and larval zebrafish. *CCS Chem.* 4, 2020–2030. <https://doi.org/10.31635/ccschem.021.202101038>.
- Goswami, N., Yao, Q., Chen, T., and Xie, J. (2016a). Mechanistic exploration and controlled synthesis of precise thiolate-gold nanoclusters. *Coord. Chem. Rev.* 329, 1–15. <https://doi.org/10.1016/j.ccr.2016.09.001>.
- Goswami, N., Yao, Q., Luo, Z., Li, J., Chen, T., and Xie, J. (2016b). Luminescent metal nanoclusters with aggregation-induced emission. *J. Phys. Chem. Lett.* 7, 962–975. <https://doi.org/10.1021/acs.jpcllett.5b02765>.
- Guan, Z.J., Zeng, J.L., Yuan, S.F., Hu, F., Lin, Y.M., and Wang, Q.M. (2018). Au₅₇Ag₅₃(C≡CPh)₄₀Br₁₂: a large nanocluster with C₁ symmetry. *Angew. Chem. Int. Ed. Engl.* 57, 5703–5707. <https://doi.org/10.1002/anie.201801261>.
- Guo, R., Wang, H., Peng, C., Shen, M., Pan, M., Cao, X., Zhang, G., and Shi, X. (2010). X-ray attenuation property of dendrimer-entrapped gold nanoparticles. *J. Phys. Chem. C* 114, 50–56. <https://doi.org/10.1021/jp9078986>.
- Guo, S., and Wang, E. (2011). Noble metal nanomaterials: controllable synthesis and application in fuel cells and analytical sensors. *Nano Today* 6, 240–264. <https://doi.org/10.1016/j.nantod.2011.04.007>.
- Hada, A.M., Craciun, A.M., Focsan, M., Borlan, R., Soritau, O., Todea, M., and Astilean, S. (2021). Folic acid functionalized gold nanoclusters for enabling targeted fluorescence imaging of human ovarian cancer cells. *Talanta* 225, 121960. <https://doi.org/10.1016/j.talanta.2020.121960>.
- Hagge, R.J., Wong, T.Z., and Coleman, R.E. (2001). Positron emission tomography: brain tumors and lung cancer. *Radiol. Clin. North Am.* 39, 871–881. [https://doi.org/10.1016/S0033-8389\(05\)70318-3](https://doi.org/10.1016/S0033-8389(05)70318-3).
- Hainfeld, J.F., Slatkin, D.N., Focella, T.M., and Smilowitz, H.M. (2006). Gold nanoparticles: a new X-ray contrast agent. *Br. J. Radiol.* 79, 248–253. <https://doi.org/10.1259/bjr/13169882>.
- Hallouard, F., Anton, N., Choquet, P., Constantinesco, A., and Vandamme, T. (2010). Iodinated blood pool contrast media for preclinical X-ray imaging applications—a review. *Biomaterials* 31, 6249–6268. <https://doi.org/10.1016/j.biomaterials.2010.04.066>.
- Han, L., Xia, J.M., Hai, X., Shu, Y., Chen, X.W., and Wang, J.H. (2017). Protein-stabilized gadolinium oxide-gold nanoclusters hybrid for multimodal imaging and drug delivery. *ACS Appl. Mater. Interfaces* 9, 6941–6949. <https://doi.org/10.1021/acsami.7b00246>.
- Han, W., Yang, W., Gao, F., Cai, P., Wang, J., Wang, S., Xue, J., Gao, X., and Liu, Y. (2020a). Iodine-124 labeled gold nanoclusters for positron emission tomography imaging in lung cancer model. *J. Nanosci. Nanotechnol.* 20, 1375–1382. <https://doi.org/10.1166/jnn.2020.17169>.
- Han, R., Zhao, M., Wang, Z., Liu, H., Zhu, S., Huang, L., Wang, Y., Wang, L., Hong, Y., Sha, Y., and Jiang, Y. (2020b). Super-efficient *in vivo* two-photon photodynamic therapy with a gold nanocluster as a type I photosensitizer. *ACS Nano* 14, 9532–9544. <https://doi.org/10.1021/acsnano.9b05169>.
- He, K., Yu, S., Wang, X., Li, D., Chen, J., Zhong, H., Xu, Q., Wu, Y.-X., and Gan, N. (2021). The fabrication of transferrin-modified two-photon gold nanoclusters with near-infrared fluorescence and their application in bioimaging. *Chem. Commun.* 57, 10391–10394. <https://doi.org/10.1039/d1cc03368a>.
- Higbee-Dempsey, E., Amirshaghghi, A., Case, M.J., Miller, J., Busch, T.M., and Tsourkas, A. (2019). Indocyanine green-coated gold nanoclusters for photoacoustic imaging and photothermal therapy. *Adv. Ther.* 2, 1900088. <https://doi.org/10.1002/adtp.201900088>.
- Hou, W., Xia, F., Alfranca, G., Yan, H., Zhi, X., Liu, Y., Peng, C., Zhang, C., de la Fuente, J.M., and Cui, D. (2017). Nanoparticles for multi-modality cancer diagnosis: simple protocol for self-assembly of gold nanoclusters mediated by gadolinium ions. *Biomaterials* 120, 103–114. <https://doi.org/10.1016/j.biomaterials.2016.12.027>.
- Hu, L., Han, S., Parveen, S., Yuan, Y., Zhang, L., and Xu, G. (2012). Highly sensitive fluorescent detection of trypsin based on BSA-stabilized gold nanoclusters. *Biosens. Bioelectron.* 32, 297–299. <https://doi.org/10.1016/j.bios.2011.12.007>.
- Hu, J., Gao, G., He, M., Yin, Q., Gao, X., Xu, H., and Sun, T. (2020). Optimal route of gold nanoclusters administration in mice targeting Parkinson's disease. *Nanomedicine* 15, 563–580. <https://doi.org/10.2217/nnm-2019-0268>.
- Huang, P., Lin, J., Li, W., Rong, P., Wang, Z., Wang, S., Wang, X., Sun, X., Aronova, M., Niu, G., et al. (2013). Biodegradable gold nanovesicles with an ultrastrong plasmonic coupling effect for photoacoustic imaging and photothermal therapy. *Angew. Chem. Int. Ed. Engl.* 52, 13958–13964. <https://doi.org/10.1002/anie.201308986>.
- Huk, W.J., and Gademann, G. (1984). Magnetic resonance imaging (MRI): method and early clinical experiences in diseases of the central nervous system. *Neurosurg. Rev.* 7, 259–280. <https://doi.org/10.1007/bf01892907>.
- Jia, M., Mi, W., Guo, S., Yang, Q.Z., Jin, Y., and Shao, N. (2020). Peptide-capped functionalized Ag/Au bimetal nanoclusters with enhanced red fluorescence for lysosome-targeted imaging of hypochlorite in living cells. *Talanta* 216, 120926. <https://doi.org/10.1016/j.talanta.2020.120926>.
- Jiang, X., Wang, X., Yao, C., Zhu, S., Liu, L., Liu, R., and Li, L. (2019). Surface-engineered gold nanoclusters with biological assembly-amplified emission for multimode imaging. *J. Phys. Chem. Lett.* 10, 5237–5243. <https://doi.org/10.1021/acs.jpcllett.9b02046>.
- Jin, R., Zeng, C., Zhou, M., and Chen, Y. (2016). Atomically precise colloidal metal nanoclusters and nanoparticles: fundamentals and opportunities. *Chem. Rev.* 116, 10346–10413. <https://doi.org/10.1021/acs.chemrev.5b00703>.
- Kang, X., Chong, H., and Zhu, M. (2018). Au₂₅(SR)₁₈: the captain of the great nanocluster ship. *Nanoscale* 10, 10758–10834. <https://doi.org/10.1039/c8nr02973c>.

- Kang, X., Li, Y., Zhu, M., and Jin, R. (2020). Atomically precise alloy nanoclusters: syntheses, structures, and properties. *Chem. Soc. Rev.* 49, 6443–6514. <https://doi.org/10.1039/C9CS00633H>.
- Krishna, K.S., Tarakeshwar, P., Mujica, V., and Kumar, C.S.S.R. (2014). Chemically induced magnetism in atomically precise gold clusters. *Small* 10, 907–911. <https://doi.org/10.1002/sml.201302393>.
- Krishna Kumar, A.S., and Tseng, W.L. (2020). Perspective on recent developments of near infrared-emitting gold nanoclusters: applications in sensing and bio-imaging. *Anal. Methods* 12, 1809–1826. <https://doi.org/10.1039/d0ay00157k>.
- Kundu, S., Ghosh, B., Nandi, S., Ghosh, M., Pyne, A., Chatterjee, J., and Sarkar, N. (2020). Surface Ligand-controlled wavelength-tunable luminescence of gold nanoclusters: cellular imaging and smart fluorescent probes for amyloid detection. *ACS Appl. Bio Mater.* 3, 4282–4293. <https://doi.org/10.1021/acsabm.0c00337>.
- Lai, L., Zhao, C., Li, X., Liu, X., Jiang, H., Selke, M., and Wang, X. (2016). Fluorescent gold nanoclusters for *in vivo* target imaging of Alzheimer's disease. *RSC Adv.* 6, 30081–30088. <https://doi.org/10.1039/c6ra01027j>.
- Le, W., Cui, S., Chen, X., Zhu, H., Chen, B., and Cui, Z. (2016). Facile synthesis of Gd-functionalized gold nanoclusters as potential MRI/CT contrast agents. *Nanomaterials* 6, 65. <https://doi.org/10.3390/nano6040065>.
- Leblond, F., Davis, S.C., Valdés, P.A., and Pogue, B.W. (2010). Pre-clinical whole-body fluorescence imaging: review of instruments, methods and applications. *J. Photochem. Photobiol. B* 98, 77–94. <https://doi.org/10.1016/j.jphotobiol.2009.11.007>.
- Lee, W.I., Bae, Y., and Bard, A.J. (2004). Strong Blue Photoluminescence and ECL from OH-terminated PAMAM dendrimers in the absence of gold nanoparticles. *J. Am. Chem. Soc.* 126, 8358–8359. <https://doi.org/10.1021/ja0475914>.
- Lei, Z., Guan, Z.J., Pei, X.L., Yuan, S.F., Wan, X.K., Zhang, J.Y., and Wang, Q.M. (2016). An atomically precise Au₁₀Ag₂ nanocluster with Red-Near-IR dual emission. *Chemistry* 22, 11156–11160. <https://doi.org/10.1002/chem.201602403>.
- Li, W., and Chen, X. (2015). Gold nanoparticles for photoacoustic imaging. *Nanomedicine* 10, 299–320. <https://doi.org/10.2217/nnm.14.169>.
- Li, C.H., Kuo, T.R., Su, H.J., Lai, W.Y., Yang, P.C., Chen, J.S., Wang, D.Y., Wu, Y.C., and Chen, C.C. (2015). Fluorescence-guided probes of aptamer-targeted gold nanoparticles with computed tomography imaging accesses for *in vivo* tumor resection. *Sci. Rep.* 5, 15675. <https://doi.org/10.1038/srep15675>.
- Li, J., Chen, R., Zhang, S., Ma, Z., Luo, Z., and Gao, G. (2019a). Chiral effect at nano-bio interface: a model of chiral gold nanoparticle on amylin fibrillation. *Nanomaterials* 9, 412. <https://doi.org/10.3390/nano9030412>.
- Li, Q., Zhou, M., So, W.Y., Huang, J., Li, M., Kauffman, D.R., Cotlet, M., Higaki, T., Peteanu, L.A., Shao, Z., and Jin, R. (2019b). A monocuboctahedral series of gold nanoclusters: photoluminescence origin, large enhancement, Wide Tunability, and Structure-Property Correlation. *J. Am. Chem. Soc.* 141, 5314–5325. <https://doi.org/10.1021/jacs.8b13558>.
- Li, D., Liu, Q., Qi, Q., Shi, H., Hsu, E.C., Chen, W., Yuan, W., Wu, Y., Lin, S., Zeng, Y., et al. (2020a). Gold nanoclusters for NIR-II fluorescence imaging of bones. *Small* 16, e2003851. <https://doi.org/10.1002/sml.202003851>.
- Li, Y., Cao, Y., Wei, L., Wang, J., Zhang, M., Yang, X., Wang, W., and Yang, G. (2020b). The assembly of protein-templated gold nanoclusters for enhanced fluorescence emission and multifunctional applications. *Acta Biomater.* 101, 436–443. <https://doi.org/10.1016/j.actbio.2019.10.035>.
- Li, Y., and Jin, R. (2021). Magnetism of atomically precise gold and doped nanoclusters: delocalized spin and interparticle coupling. *J. Phys. Chem. C* 125, 15773–15784. <https://doi.org/10.1021/acs.jpcc.1c04621>.
- Li, Q., Zeman, C.J., 4th, Schatz, G.C., and Gu, X.W. (2021). Source of bright near-infrared luminescence in gold nanoclusters. *ACS Nano* 15, 16095–16105. <https://doi.org/10.1021/acsnano.1c04759>.
- Li, S., Ma, Q., Wang, C., Yang, K., Hong, Z., Chen, Q., Song, J., Song, X., and Yang, H. (2022). Near-Infrared II gold nanocluster assemblies with improved luminescence and biofate for *in vivo* ratiometric imaging of H₂S. *Anal. Chem.* 94, 2641–2647. <https://doi.org/10.1021/acs.analchem.1c05154>.
- Liang, G., and Xiao, L. (2017). Gd³⁺-Functionalized gold nanoclusters for fluorescence-magnetic resonance bimodal imaging. *Biomater. Sci.* 5, 2122–2130. <https://doi.org/10.1039/c7bm00608j>.
- Liang, G., Ye, D., Zhang, X., Dong, F., Chen, H., Zhang, S., Li, J., Shen, X., and Kong, J. (2013). One-pot synthesis of Gd³⁺-functionalized gold nanoclusters for dual model (fluorescence/magnetic resonance) imaging. *J. Mater. Chem. B* 1, 3545–3552. <https://doi.org/10.1039/c3tb20440e>.
- Lin, C.A.J., Yang, T.Y., Lee, C.H., Huang, S.H., Sperling, R.A., Zanella, M., Li, J.K., Shen, J.L., Wang, H.H., Yeh, H.I., et al. (2009). Synthesis, characterization, and bioconjugation of fluorescent gold nanoclusters toward biological labeling applications. *ACS Nano* 3, 395–401. <https://doi.org/10.1021/nn800632j>.
- Liu, H., Hong, G., Luo, Z., Chen, J., Chang, J., Gong, M., He, H., Yang, J., Yuan, X., Li, L., et al. (2019). Atomic-precision gold clusters for NIR-II imaging. *Adv. Mater.* 31, e1901015. <https://doi.org/10.1002/adma.201901015>.
- Liu, C., Zhang, X., Han, X., Fang, Y., Liu, X., Wang, X., Waterhouse, G.I.N., Xu, C., Yin, H., and Gao, X. (2020). Polypeptide-templated Au nanoclusters with red and blue fluorescence emissions for multimodal imaging of cell nuclei. *ACS Appl. Bio Mater.* 3, 1934–1943. <https://doi.org/10.1021/acsabm.9b01078>.
- Luo, Z., Yuan, X., Yu, Y., Zhang, Q., Leong, D.T., Lee, J.Y., and Xie, J. (2012). From aggregation-induced emission of Au(I)-thiolate complexes to ultrabright Au(0)@Au(I)-thiolate core-shell nanoclusters. *J. Am. Chem. Soc.* 134, 16662–16670. <https://doi.org/10.1021/ja306199p>.
- Lv, C., Yin, S., Zhang, X., Hu, J., Zhang, T., and Zhao, G. (2020). 16-Mer ferritin-like protein templated gold nanoclusters for bioimaging detection of methylmercury in the brain of living mice. *Anal. Chim. Acta* 1127, 149–155. <https://doi.org/10.1016/j.aca.2020.06.055>.
- Machac, J. (2005). Cardiac positron emission tomography imaging. *Semin. Nucl. Med.* 35, 17–36. <https://doi.org/10.1053/j.semnuclmed.2004.09.002>.
- Maity, S., Bain, D., and Patra, A. (2019). An overview on the current understanding of the photophysical properties of metal nanoclusters and their potential applications. *Nanoscale* 11, 22685–22723. <https://doi.org/10.1039/c9nr07963g>.
- Mooradian, A. (1969). Photoluminescence of metals. *Phys. Rev. Lett.* 22, 185–187. <https://doi.org/10.1103/PhysRevLett.22.185>.
- Na, H.B., Song, I.C., and Hyeon, T. (2009). Inorganic nanopores for MRI contrast agents. *Adv. Mater.* 21, 2133–2148. <https://doi.org/10.1002/adma.200802366>.
- Ndugire, W., and Yan, M. (2021). Synthesis and solution isomerization of water-soluble Au₉ nanoclusters prepared by nuclearity conversion of [Au₁₁(PPh₃)₈Cl₂]Cl. *Nanoscale* 13, 16809–16817. <https://doi.org/10.1039/d1nr04401j>.
- Ning, X., Peng, C., Li, E.S., Xu, J., Vinluan III, R.D., Yu, M., and Zheng, J. (2017). Physiological stability and renal clearance of ultrasmall zwitterionic gold nanoparticles: ligand length matters. *Appl. Mater.* 5, 053406. <https://doi.org/10.1063/1.4978381>.
- Olesiak-Banska, J., Waszkielewicz, M., Matczyszyn, K., and Samoc, M. (2016). A closer look at two-photon absorption, absorption saturation and nonlinear refraction in gold nanoclusters. *RSC Adv.* 6, 98748–98752. <https://doi.org/10.1039/c6ra20610g>.
- Pan, Y., Neuss, S., Leifert, A., Fischler, M., Wen, F., Simon, U., Schmid, G., Brandau, W., and Jahn-Dechent, W. (2007). Size-dependent cytotoxicity of gold nanoparticles. *Small* 3, 1941–1949. <https://doi.org/10.1002/sml.200700378>.
- Pan, Y., Li, Q., Zhou, Q., Zhang, W., Yue, P., Xu, C., Qin, X., Yu, H., and Zhu, M. (2018). Cancer cell specific fluorescent methionine protected gold nanoclusters for *in-vitro* cell imaging studies. *Talanta* 188, 259–265. <https://doi.org/10.1016/j.talanta.2018.05.079>.
- Pan, S., Zhou, J., Liu, W., Ye, Y., Chen, G., Xu, J., Qian, Z., Chen, J., and Feng, H. (2019). Viscosity-sensitive thiolated gold nanoclusters with diffusion-controlled emission for intracellular viscosity imaging. *Analyst* 144, 4483–4487. <https://doi.org/10.1039/c9an01035a>.
- Peng, C., Wang, H., Guo, R., Shen, M., Cao, X., Zhu, M., Zhang, G., and Shi, X. (2011). Acetylation of dendrimer-entrapped gold nanoparticles: synthesis, stability, and X-ray attenuation properties. *J. Appl. Polym. Sci.* 119, 1673–1682. <https://doi.org/10.1002/app.32845>.

- Peng, C., Zheng, L., Chen, Q., Shen, M., Guo, R., Wang, H., Cao, X., Zhang, G., and Shi, X. (2012). PEGylated dendrimer-entrapped gold nanoparticles for *in vivo* blood pool and tumor imaging by computed tomography. *Biomaterials* 33, 1107–1119. <https://doi.org/10.1016/j.biomaterials.2011.10.052>.
- Peng, J., and Liang, X. (2019). Progress in research on gold nanoparticles in cancer management. *Medicine* 98, e15311. <https://doi.org/10.1097/MD.00000000000015311>.
- Petersen, A.L., Binderup, T., Rasmussen, P., Henriksen, J.R., Elema, D.R., Kjær, A., and Andresen, T.L. (2011). ⁶⁴Cu loaded liposomes as positron emission tomography imaging agents. *Biomaterials* 32, 2334–2341. <https://doi.org/10.1016/j.biomaterials.2010.11.059>.
- Polavarapu, L., Manna, M., and Xu, Q.-H. (2011). Biocompatible glutathione capped gold clusters as one- and two-photon excitation fluorescence contrast agents for live cells imaging. *Nanoscale* 3, 429–434. <https://doi.org/10.1039/c0nr00458h>.
- Porret, E., Le Guével, X., and Coll, J.L. (2020). Gold nanoclusters for biomedical applications: toward *in vivo* studies. *J. Mater. Chem. B* 8, 2216–2232. <https://doi.org/10.1039/c9tb02767j>.
- Pyo, K., Thanthirige, V.D., Kwak, K., Pandurangan, P., Ramakrishna, G., and Lee, D. (2015). Ultrabright luminescence from gold nanoclusters: rigidifying the Au(I)-thiolate shell. *J. Am. Chem. Soc.* 137, 8244–8250. <https://doi.org/10.1021/jacs.5b04210>.
- Pyo, K., Thanthirige, V.D., Yoon, S.Y., Ramakrishna, G., and Lee, D. (2016). Enhanced luminescence of Au₂₂(SG)₁₈ nanoclusters via rational surface engineering. *Nanoscale* 8, 20008–20016. <https://doi.org/10.1039/c6nr07660b>.
- Raju, S., Manalele Joseph, M., Kuttanpillai, R.P., Padinjathil, H., Gopalakrishnan Nair Usha, P., and Therakathil Thankappan Nair, S. (2020). Polysaccharide enabled biogenic fabrication of pH sensing fluorescent gold nanoclusters as a biocompatible tumor imaging probe. *Mikrochim. Acta* 187, 246. <https://doi.org/10.1007/s00604-020-4189-8>.
- Ramakrishna, G., Varnavski, O., Kim, J., Lee, D., and Goodson, T. (2008). Quantum-sized gold clusters as efficient two-photon absorbers. *J. Am. Chem. Soc.* 130, 5032–5033. <https://doi.org/10.1021/ja800341v>.
- Santos, O., Cancino-Bernardi, J., Pincela Lins, P.M., Sampaio, D., Pavan, T., and Zucolotto, V. (2021). Near-Infrared photoactive theragnostic gold nanoflowers for photoacoustic imaging and hyperthermia. *ACS Appl. Bio Mater.* 4, 6780–6790. <https://doi.org/10.1021/acsabm.1c00519>.
- Schrand, A.M., Rahman, M.F., Hussain, S.M., Schlager, J.J., Smith, D.A., and Syed, A.F. (2010). Metal-based nanoparticles and their toxicity assessment. *Wiley Interdiscip. Rev. Nanomed. Nanobiotechnol.* 2, 544–568. <https://doi.org/10.1002/wnan.103>.
- Sha, Q., Guan, R., Su, H., Zhang, L., Liu, B.F., Hu, Z., and Liu, X. (2020). Carbohydrate-protein template synthesized high mannose loading gold nanoclusters: a powerful fluorescence probe for sensitive concanavalin a detection and specific breast cancer cell imaging. *Talanta* 218, 121130. <https://doi.org/10.1016/j.talanta.2020.121130>.
- Shen, D., Henry, M., Trouillet, V., Comby-Zerbino, C., Bertorelle, F., Sancey, L., Antoine, R., Coll, J.L., Jossierand, V., and Le Guével, X. (2017). Zwitterion functionalized gold nanoclusters for multimodal near infrared fluorescence and photoacoustic imaging. *Apl. Mater.* 5, 053404. <https://doi.org/10.1063/1.4977203>.
- Shen, J., Xiao, Q., Sun, P., Feng, J., Xin, X., Yu, Y., and Qi, W. (2021). Self-assembled chiral phosphorescent microflowers from Au nanoclusters with dual-mode pH sensing and information encryption. *ACS Nano* 15, 4947–4955. <https://doi.org/10.1021/acsnano.0c09766>.
- Shichibu, Y., Negishi, Y., Tsukuda, T., and Teranishi, T. (2005). Large-scale synthesis of thiolated Au₂₅ clusters via ligand exchange reactions of phosphine-stabilized Au₁₁ clusters. *J. Am. Chem. Soc.* 127, 13464–13465. <https://doi.org/10.1021/ja053915s>.
- Simpson, C.A., Salleng, K.J., Cliffl, D.E., and Feldheim, D.L. (2013). *In vivo* toxicity, biodistribution, and clearance of glutathione-coated gold nanoparticles. *Nanomedicine* 9, 257–263. <https://doi.org/10.1016/j.nano.2012.06.002>.
- Song, X.R., Goswami, N., Yang, H.H., and Xie, J. (2016). Functionalization of metal nanoclusters for biomedical applications. *Analyst* 141, 3126–3140. <https://doi.org/10.1039/c6an00773b>.
- Song, X., Zhu, W., Ge, X., Li, R., Li, S., Chen, X., Song, J., Xie, J., Chen, X., and Yang, H. (2021). A new class of NIR-II gold nanocluster-based protein biolabels for *in vivo* tumor-targeted imaging. *Angew. Chem. Int. Ed. Engl.* 60, 1306–1312. <https://doi.org/10.1002/anie.202010870>.
- Sugiuchi, M., Maeaba, J., Okubo, N., Iwamura, M., Nozaki, K., and Konishi, K. (2017). Aggregation-induced fluorescence-to-phosphorescence switching of molecular gold clusters. *J. Am. Chem. Soc.* 139, 17731–17734. <https://doi.org/10.1021/jacs.7b10201>.
- Sultan, D., Li, W., Detering, L., Heo, G.S., Luehmann, H.P., Kreisel, D., and Liu, Y. (2021). Assessment of ultrasmall nanocluster for early and accurate detection of atherosclerosis using positron emission tomography/computed tomography. *Nanomedicine* 36, 102416. <https://doi.org/10.1016/j.nano.2021.102416>.
- Sun, G., Zhou, L., Liu, Y., and Zhao, Z. (2013). Biocompatible GdIII-functionalized fluorescent gold nanoclusters for optical and magnetic resonance imaging. *New J. Chem.* 37, 1028–1035. <https://doi.org/10.1039/c3nj00052d>.
- Sun, Y., Wu, J., Wang, C., Zhao, Y., and Lin, Q. (2017). Tunable near-infrared fluorescent gold nanoclusters: temperature sensor and targeted bioimaging. *New J. Chem.* 41, 5412–5419. <https://doi.org/10.1039/c7nj00175d>.
- Tamada, T., Ito, K., Sone, T., Yamamoto, A., Yoshida, K., Kakuba, K., Tanimoto, D., Higashi, H., and Yamashita, T. (2009). Dynamic contrast-enhanced magnetic resonance imaging of abdominal solid organ and major vessel: comparison of enhancement effect between Gd-EOB-DTPA and Gd-DTPA. *J. Magn. Reson. Imaging.* 29, 636–640. <https://doi.org/10.1002/jmri.21689>.
- Tang, L., Zeng, X., Zhou, H., Gui, C., Luo, Q., Zhou, W., Wu, J., Li, Q., Li, Y., and Xiao, Y. (2021). Theranostic Gold Nanoclusters for NIR-II imaging and photodynamic therapy. *Chem. Res. Chin. Univ.* 37, 934–942. <https://doi.org/10.1007/s40242-021-1117-3>.
- Tian, S., Liao, L., Yuan, J., Yao, C., Chen, J., Yang, J., and Wu, Z. (2016). Structures and magnetism of mono-palladium and mono-platinum doped Au₂₅(PET)₁₈ nanoclusters. *Chem. Commun.* 52, 9873–9876. <https://doi.org/10.1039/C6CC02698B>.
- Tian, Y., Wei, M., Wang, L., Hong, Y., Luo, D., and Sha, Y. (2021). Two-photon time-gated *in vivo* imaging of dihydrolipoic-acid-decorated gold nanoclusters. *Materials* 14, 7744. <https://doi.org/10.3390/ma14247744>.
- Trudel, S. (2011). Unexpected magnetism in gold nanostructures: making gold even more attractive. *Gold Bull.* 44, 3–13. <https://doi.org/10.1007/s13404-010-0002-5>.
- Tsvirkun, D., Ben-Nun, Y., Merquiol, E., Zlotver, I., Meir, K., Weiss-Sadan, T., Matok, I., Popovtzer, R., and Blum, G. (2018). CT imaging of enzymatic activity in cancer using covalent probes reveal a size-dependent pattern. *J. Am. Chem. Soc.* 140, 12010–12020. <https://doi.org/10.1021/jacs.8b05817>.
- Ulloa, J.A., Lorusso, G., Evangelisti, M., Camón, A., Barberá, J., and Serrano, J.L. (2021). Magnetism of dendrimer-coated gold nanoparticles: a size and functionalization study. *J. Phys. Chem. C Nanomater. Interfaces* 125, 20482–20487. <https://doi.org/10.1021/acs.jpcc.1c04213>.
- Upputuri, P.K., and Pramanik, M. (2020). Recent advances in photoacoustic contrast agents for *in vivo* imaging. *Wiley Interdiscip. Rev. Nanomed. Nanobiotechnol.* 12, e1618. <https://doi.org/10.1002/wnan.1618>.
- Vivo-Llorca, G., Morellá-Aucejo, Á., García-Fernández, A., Díez, P., Llopis-Lorente, A., Orzáez, M., and Martínez-Mañez, R. (2022). Horseradish peroxidase-functionalized gold nanoconjugates for breast cancer treatment based on enzyme prodrug therapy. *Int. J. Nanomedicine* 17, 409–422. <https://doi.org/10.2147/IJN.S323802>.
- Wang, G., Huang, T., Murray, R.W., Menard, L., and Nuzzo, R.G. (2005). Near-IR luminescence of monolayer-protected metal clusters. *J. Am. Chem. Soc.* 127, 812–813. <https://doi.org/10.1021/ja0452471>.
- Wang, L.V., and Hu, S. (2012). Photoacoustic tomography: *in vivo* imaging from organelles to organs. *Science* 335, 1458–1462. <https://doi.org/10.1126/science.1216210>.
- Wang, J., Zhang, G., Li, Q., Jiang, H., Liu, C., Amatore, C., and Wang, X. (2013). *In vivo* self-bio-imaging of tumors through *in situ* biosynthesized fluorescent gold nanoclusters. *Sci. Rep.* 3, 1157. <https://doi.org/10.1038/srep01157>.
- Wang, C., Yao, Y., and Song, Q. (2015a). Gold nanoclusters decorated with magnetic iron oxide nanoparticles for potential multimodal

- optical/magnetic resonance imaging. *J. Mater. Chem. C* 3, 5910–5917. <https://doi.org/10.1039/c5tc00290g>.
- Wang, S., Jin, S., Yang, S., Chen, S., Song, Y., Zhang, J., and Zhu, M. (2015b). Total structure determination of surface doping [Ag₄₆Au₂₄(SR)₃₂](BPh₄)₂ nanocluster and its structure-related catalytic property. *Sci. Adv.* 1, e1500441. <https://doi.org/10.1126/sciadv.1500441>.
- Wang, Y., Xu, C., Zhai, J., Gao, F., Liu, R., Gao, L., Zhao, Y., Chai, Z., and Gao, X. (2015c). Label-free Au cluster used for *in vivo* 2D and 3D computed tomography of murine kidneys. *Anal. Chem.* 87, 343–345. <https://doi.org/10.1021/ac503887c>.
- Wang, L.V., and Yao, J. (2016). A practical guide to photoacoustic tomography in the life sciences. *Nat. Methods* 13, 627–638. <https://doi.org/10.1038/nmeth.3925>.
- Wang, Y., Hu, L., Li, L., and Zhu, J.-J. (2017). Fluorescent gold nanoclusters: promising fluorescent probes for sensors and bioimaging. *J. Anal. Test.* 1, 13–19. <https://doi.org/10.1007/s41664-017-0015-7>.
- Wang, J., Wu, M., Chang, J., Li, L., Guo, Q., Hao, J., Peng, Q., Zhang, B., Zhang, X., and Li, X. (2019). Scavenger receptor-AI-targeted ultrasmall gold nanoclusters facilitate *in vivo* MR and *ex vivo* fluorescence dual-modality visualization of vulnerable atherosclerotic plaques. *Nanomedicine* 19, 81–94. <https://doi.org/10.1016/j.nano.2019.04.003>.
- Wang, W., Kong, Y., Jiang, J., Xie, Q., Huang, Y., Li, G., Wu, D., Zheng, H., Gao, M., Xu, S., et al. (2020). Engineering the protein corona structure on gold nanoclusters enables red-shifted emissions in the second near-infrared window for gastrointestinal imaging. *Angew. Chem. Int. Ed. Engl.* 59, 22431–22435. <https://doi.org/10.1002/anie.202010089>.
- Wang, Y., Fadhel, M.N., Hysi, E., Pastenak, M., Sathiyamoorthy, K., and Kolios, M.C. (2021). *In vivo* spectroscopic photoacoustic imaging and laser-induced nanoparticle vaporization for anti-HER2 breast cancer. *J. Biophotonics* 14, e202100099. <https://doi.org/10.1002/jbio.202100099>.
- Wang, Z., He, L., Che, S., Xing, H., Guan, L., Yang, Z., Li, X., Zvyagin, A.V., Lin, Q., and Qu, W. (2022). AuNCs-LHRHa nano-system for FL/CT dual-mode imaging and photothermal therapy of targeted prostate cancer. *J. Mater. Chem. B* 10, 5182–5190. <https://doi.org/10.1039/d2tb00531j>.
- Werner, E.J., Datta, A., Jocher, C.J., and Raymond, K.N. (2008). High-relaxivity MRI contrast agents: where coordination chemistry meets medical imaging. *Angew. Chem. Int. Ed. Engl.* 47, 8568–8580. <https://doi.org/10.1002/anie.200800212>.
- Window, P.S., and Ackerson, C.J. (2020). Superatom paramagnetism in Au₁₀₂(SR)₄₄²⁺ oxidation states. *Inorg. Chem.* 59, 3509–3512. <https://doi.org/10.1021/acs.inorgchem.9b02787>.
- Wu, Z., and Jin, R. (2010). On the ligand's role in the fluorescence of gold nanoclusters. *Nano Lett.* 10, 2568–2573. <https://doi.org/10.1021/nl101225f>.
- Wu, X., He, X., Wang, K., Xie, C., Zhou, B., and Qing, Z. (2010). Ultrasmall near-infrared gold nanoclusters for tumor fluorescence imaging *in vivo*. *Nanoscale* 2, 2244–2249. <https://doi.org/10.1039/c0nr00359j>.
- Wu, D., Ylli, D., Heimlich, S.L., Burman, K.D., Wartofsky, L., and Van Nostrand, D. (2019). ¹²⁴I positron emission tomography/computed tomography versus conventional radioiodine imaging in differentiated thyroid cancer: a review. *Thyroid* 29, 1523–1535. <https://doi.org/10.1089/thy.2018.0598>.
- Wu, Z., Yao, Q., Chai, O.J.H., Ding, N., Xu, W., Zang, S., and Xie, J. (2020). Unraveling the impact of gold(I)-thiolate motifs on the aggregation-induced emission of gold nanoclusters. *Angew. Chem. Int. Ed. Engl.* 59, 9934–9939. <https://doi.org/10.1002/anie.201916675>.
- Wu, H., Fang, Y.G., Anumula, R., Andrew, G.N., Cui, G., Fang, W., Luo, Z., and Yao, J. (2021). A mono-copper doped undeca-gold cluster with up-converted and anti-Stokes emissions of fluorescence and phosphorescence. *Nanoscale* 13, 5300–5306. <https://doi.org/10.1039/d0nr07624d>.
- Xia, F., Hou, W., Zhang, C., Zhi, X., Cheng, J., de la Fuente, J.M., Song, J., and Cui, D. (2018). pH-responsive gold nanoclusters-based nanoprobe for lung cancer targeted near-infrared fluorescence imaging and chemo-photodynamic therapy. *Acta Biomater.* 68, 308–319. <https://doi.org/10.1016/j.actbio.2017.12.034>.
- Xia, J., Wang, X., Zhu, S., Liu, L., and Li, L. (2019). Gold nanocluster-decorated nanocomposites with enhanced emission and reactive oxygen species generation. *ACS Appl. Mater. Interfaces* 11, 7369–7378. <https://doi.org/10.1021/acsami.8b19679>.
- Xie, J., Zheng, Y., and Ying, J.Y. (2009). Protein-directed synthesis of highly fluorescent gold nanoclusters. *J. Am. Chem. Soc.* 131, 888–889. <https://doi.org/10.1021/ja806804u>.
- Xu, C., Tung, G.A., and Sun, S. (2008). Size and concentration effect of gold nanoparticles on X-ray attenuation as measured on computed tomography. *Chem. Mater.* 20, 4167–4169. <https://doi.org/10.1021/cm8008418>.
- Xu, J.X., Yuan, Y., Zou, S., Chen, O., and Zhang, D. (2019). A divide-and-conquer strategy for quantification of light absorption, scattering, and emission properties of fluorescent nanomaterials in solutions. *Anal. Chem.* 91, 8540–8548. <https://doi.org/10.1021/acs.analchem.9b01803>.
- Yan, G., Liu, M., Cheng, Y., Xue, F., An, L., and Tian, Q. (2021). Small Au nanorods-MnO₂ sheet aggregation with enhanced photoacoustic imaging for tumor. *Mater. Lett.* 304, 130592. <https://doi.org/10.1016/j.matlet.2021.130592>.
- Yang, J., Liao, L., Wang, J., Zhu, X., Xu, A., and Wu, Z. (2016). Size-dependent cytotoxicity of thiolated silver nanoparticles rapidly probed by using differential pulse voltammetry. *Chemelectrochem* 3, 1197–1200. <https://doi.org/10.1002/celec.201600211>.
- Yang, J., Wang, T., Zhao, L., Rajasekhar, V.K., Joshi, S., Andreou, C., Pal, S., Hsu, H.T., Zhang, H., Cohen, I.J., et al. (2020a). Gold/alpha-lactalbumin nanoprobe for the imaging and treatment of breast cancer. *Nat. Biomed. Eng.* 4, 686–703. <https://doi.org/10.1038/s41551-020-0584-z>.
- Yang, Y., Yu, Y., Chen, H., Meng, X., Ma, W., Yu, M., Li, Z., Li, C., Liu, H., Zhang, X., et al. (2020b). Illuminating platinum transportation while maximizing therapeutic efficacy by gold nanoclusters via simultaneous Near-Infrared-I/II imaging and glutathione scavenging. *ACS Nano* 14, 13536–13547. <https://doi.org/10.1021/acsnano.0c05541>.
- Yang, Z., Zhao, Y., Hao, Y., Li, X., Zvyagin, A.V., Whittaker, A.K., Cui, Y., Yang, B., Lin, Q., and Li, Y. (2021). Ultrasmall red fluorescent gold nanoclusters for highly biocompatible and long-time nerve imaging. *Part. Part. Syst. Charact.* 38, 2100001. <https://doi.org/10.1002/ppsc.202100001>.
- Yang, J., Yang, F., Zhang, C., He, X., and Jin, R. (2022). Metal nanoclusters as biomaterials for bioapplications: atomic precision as the next goal. *ACS Mater. Lett.* 4, 1279–1296. <https://doi.org/10.1021/acsmaterialslett.2c00237>.
- Yao, C., Lin, Y.j., Yuan, J., Liao, L., Zhu, M., Weng, L.h., Yang, J., and Wu, Z. (2015). Mono-cadmium vs mono-mercury doping of Au₂₅ nanoclusters. *J. Am. Chem. Soc.* 137, 15350–15353. <https://doi.org/10.1021/jacs.5b09627>.
- Yu, M., and Zheng, J. (2015). Clearance pathways and tumor targeting of imaging nanoparticles. *ACS Nano* 9, 6655–6674. <https://doi.org/10.1021/acsnano.5b01320>.
- Yu, Y., Chen, X., Yao, Q., Yu, Y., Yan, N., and Xie, J. (2013). Scalable and precise synthesis of thiolated Au_{10–12}, Au₁₅, Au₁₈, and Au₂₅ nanoclusters via pH controlled CO reduction. *Chem. Mater.* 25, 946–952. <https://doi.org/10.1021/cm304098x>.
- Yu, Y., Luo, Z., Chevrier, D.M., Leong, D.T., Zhang, P., Jiang, D.E., and Xie, J. (2014). Identification of a highly luminescent Au₂₂(SG)₁₈ nanocluster. *J. Am. Chem. Soc.* 136, 1246–1249. <https://doi.org/10.1021/ja411643u>.
- Yu, Z., Munsier, B., Wegner, K.D., Henry, M., Chovelon, B., Desroches-Castan, A., Fertin, A., Resch-Genger, U., Bailly, S., Coll, J.L., et al. (2020). High-resolution shortwave infrared imaging of vascular disorders using gold nanoclusters. *ACS Nano* 14, 4973–4981. <https://doi.org/10.1021/acsnano.0c01174>.
- Zelmer, A., and Ward, T.H. (2013). Noninvasive fluorescence imaging of small animals. *J. Microsc.* 252, 8–15. <https://doi.org/10.1111/jmi.12063>.
- Zhai, Q., Xing, H., Fan, D., Zhang, X., Li, J., and Wang, E. (2018). Gold-silver bimetallic nanoclusters with enhanced fluorescence for highly selective and sensitive detection of glutathione. *Sensor. Actuator. B Chem.* 273, 1827–1832. <https://doi.org/10.1016/j.snb.2018.05.145>.
- Zhang, A., Tu, Y., Qin, S., Li, Y., Zhou, J., Chen, N., Lu, Q., and Zhang, B. (2012a). Gold nanoclusters as contrast agents for fluorescent and X-ray dual-modality imaging. *J. Colloid Interface Sci.* 372, 239–244. <https://doi.org/10.1016/j.jcis.2012.01.005>.
- Zhang, X.D., Wu, D., Shen, X., Liu, P.X., Fan, F.Y., and Fan, S.J. (2012b). *In vivo* renal clearance, biodistribution, toxicity of gold nanoclusters.

- Biomaterials 33, 4628–4638. <https://doi.org/10.1016/j.biomaterials.2012.03.020>.
- Zhang, C., Zhou, Z., Qian, Q., Gao, G., Li, C., Feng, L., Wang, Q., and Cui, D. (2013). Glutathione-capped fluorescent gold nanoclusters for dual-modal fluorescence/X-ray computed tomography imaging. *J. Mater. Chem. B* 1, 5045–5053. <https://doi.org/10.1039/c3tb20784f>.
- Zhang, L., and Wang, E. (2014). Metal nanoclusters: new fluorescent probes for sensors and bioimaging. *Nano Today* 9, 132–157. <https://doi.org/10.1016/j.nantod.2014.02.010>.
- Zhang, X.D., Chen, J., Luo, Z., Wu, D., Shen, X., Song, S.S., Sun, Y.M., Liu, P.X., Zhao, J., Huo, S., et al. (2014). Enhanced tumor accumulation of sub-2 nm gold nanoclusters for cancer radiation therapy. *Adv. Healthc. Mater.* 3, 133–141. <https://doi.org/10.1002/adhm.201300189>.
- Zhang, C., Li, C., Liu, Y., Zhang, J., Bao, C., Liang, S., Wang, Q., Yang, Y., Fu, H., Wang, K., and Cui, D. (2015a). Gold nanoclusters-based nanoprobe for simultaneous fluorescence imaging and targeted photodynamic therapy with superior penetration and retention behavior in tumors. *Adv. Funct. Mater.* 25, 1314–1325. <https://doi.org/10.1002/adfm.201403095>.
- Zhang, W., Ye, J., Zhang, Y., Li, Q., Dong, X., Jiang, H., and Wang, X. (2015b). One-step facile synthesis of fluorescent gold nanoclusters for rapid bio-imaging of cancer cells and small animals. *RSC Adv.* 5, 63821–63826. <https://doi.org/10.1039/c5ra11321k>.
- Zhang, L., and Han, F. (2018). Protein coated gold nanoparticles as template for the directed synthesis of highly fluorescent gold nanoclusters. *Nanotechnology* 29, 165702. <https://doi.org/10.1088/1361-6528/aaae47>.
- Zhang, X., Chen, M., Zhang, Y., Hou, Y., Wu, Y., Yao, M., Li, L., Shi, L., Liu, T., Hu, B., et al. (2020). Monoclonal-antibody-templated gold nanoclusters for HER2 receptors targeted fluorescence imaging. *ACS Appl. Bio Mater.* 3, 7061–7066. <https://doi.org/10.1021/acsbm.0c00905>.
- Zhang, Y., Yan, H., Su, R., Li, P., Wen, F., Lv, Y., Cai, J., and Su, W. (2022). Photoactivated multifunctional nanoplateform based on lysozyme-Au nanoclusters-curcumin conjugates with FRET effect and multi-amplified antimicrobial activity. *J. Drug Deliv. Sci. Technol.* 74, 103548. <https://doi.org/10.1016/j.jddst.2022.103548>.
- Zhao, Y., Sultan, D., Detering, L., Cho, S., Sun, G., Pierce, R., Wooley, K.L., and Liu, Y. (2014a). Copper-64-alloyed gold nanoparticles for cancer imaging: improved radiolabel stability and diagnostic accuracy. *Angew. Chem. Int. Ed. Engl.* 53, 156–159. <https://doi.org/10.1002/anie.201308494>.
- Zhao, Y., Sultan, D., Detering, L., Luehmann, H., and Liu, Y. (2014b). Facile synthesis, pharmacokinetic and systemic clearance evaluation, and positron emission tomography cancer imaging of ⁶⁴Cu-Au alloy nanoclusters. *Nanoscale* 6, 13501–13509. <https://doi.org/10.1039/c4nr04569f>.
- Zhao, C., Du, T., Rehman, F.U., Lai, L., Liu, X., Jiang, X., Li, X., Chen, Y., Zhang, H., Sun, Y., et al. (2016a). Biosynthesized gold nanoclusters and iron complexes as scaffolds for multimodal cancer bioimaging. *Small* 12, 6255–6265. <https://doi.org/10.1002/smll.201602526>.
- Zhao, Y., Detering, L., Sultan, D., Cooper, M.L., You, M., Cho, S., Meier, S.L., Luehmann, H., Sun, G., Rettig, M., et al. (2016b). Gold nanoclusters doped with ⁶⁴Cu for CXCR4 positron emission tomography imaging of breast cancer and metastasis. *ACS Nano* 10, 5959–5970. <https://doi.org/10.1021/acsnano.6b01326>.
- Zhao, Y., You, M., Detering, L., Sultan, D., Luehmann, H., and Liu, Y. (2021). Chemokine receptor 2 targeted gold nanocluster imaging triple negative breast cancer with positron emission tomography. *Part. Part. Syst. Charact.* 38, 2000287. <https://doi.org/10.1002/ppsc.202000287>.
- Zheng, J., Zhang, C., and Dickson, R.M. (2004). Highly fluorescent, water-soluble, size-tunable gold quantum dots. *Phys. Rev. Lett.* 93, 077402. <https://doi.org/10.1103/PhysRevLett.93.077402>.
- Zheng, Y., Lai, L., Liu, W., Jiang, H., and Wang, X. (2017). Recent advances in biomedical applications of fluorescent gold nanoclusters. *Adv. Colloid Interface Sci.* 242, 1–16. <https://doi.org/10.1016/j.cis.2017.02.005>.
- Zheng, B., Wu, Q., Jiang, Y., Hou, M., Zhang, P., Liu, M., Zhang, L., Li, B., and Zhang, C. (2021a). One-pot synthesis of ⁶⁸Ga-doped ultrasmall gold nanoclusters for PET/CT imaging of tumors. *Mater. Sci. Eng. C Mater. Biol. Appl.* 128, 112291. <https://doi.org/10.1016/j.msec.2021.112291>.
- Zheng, L., Zhu, R., Chen, L., Fu, Q., Li, J., Chen, C., Song, J., and Yang, H. (2021b). X-ray sensitive high-Z metal nanocrystals for cancer imaging and therapy. *Nano Res.* 14, 3744–3755. <https://doi.org/10.1007/s12274-021-3337-8>.
- Zheng, Y., Wu, J., Jiang, H., and Wang, X. (2021c). Gold nanoclusters for theranostic applications. *Coord. Chem. Rev.* 431, 213689. <https://doi.org/10.1016/j.ccr.2020.213689>.
- Zhou, C., Long, M., Qin, Y., Sun, X., and Zheng, J. (2011). Luminescent gold nanoparticles with efficient renal clearance. *Angew. Chem. Int. Ed. Engl.* 50, 3168–3172. <https://doi.org/10.1002/anie.201007321>.
- Zhou, C., Hao, G., Thomas, P., Liu, J., Yu, M., Sun, S., Oz, O.K., Sun, X., and Zheng, J. (2012). Near-infrared emitting radioactive gold nanoparticles with molecular pharmacokinetics. *Angew. Chem. Int. Ed. Engl.* 51, 10118–10122. <https://doi.org/10.1002/anie.201203031>.
- Zhou, Z., Zhang, C., Qian, Q., Ma, J., Huang, P., Zhang, X., Pan, L., Gao, G., Fu, H., Fu, S., et al. (2013). Folic acid-conjugated silica capped gold nanoclusters for targeted fluorescence/X-ray computed tomography imaging. *J. Nanobiotechnology* 11, 17. <https://doi.org/10.1186/1477-3155-11-17>.
- Zhu, M., Aikens, C.M., Hendrich, M.P., Gupta, R., Qian, H., Schatz, G.C., and Jin, R. (2009). Reversible switching of magnetism in thiolate-protected Au₂₅ superatoms. *J. Am. Chem. Soc.* 131, 2490–2492. <https://doi.org/10.1021/ja809157f>.
- Zhu, H., Li, J., Wang, J., and Wang, E. (2019). Lighting up the gold nanoclusters via host-guest recognition for high-efficiency antibacterial performance and imaging. *ACS Appl. Mater. Interfaces* 11, 36831–36838. <https://doi.org/10.1021/acsomega.9b11026>.
- Zhu, S., Wang, X., Cong, Y., and Li, L. (2020a). Regulating the optical properties of gold nanoclusters for biological applications. *ACS Omega* 5, 22702–22707. <https://doi.org/10.1021/acsomega.0c03218>.
- Zhu, S., Wang, X., Liu, L., and Li, L. (2020b). Gold nanocluster grafted conjugated polymer nanoparticles for cancer cell imaging and photothermal killing. *Colloids Surf. A Physicochem. Eng. Asp.* 597, 124764. <https://doi.org/10.1016/j.colsurfa.2020.124764>.
- Ziegler, S.I. (2005). Positron emission tomography: principles, technology, and recent developments. *Nucl. Phys.* 752, 679–687. <https://doi.org/10.1016/j.nuclphysa.2005.02.067>.